THE “ODD” BEHAVIOR OF OZONE PHOTODISSOCIATION

A Dissertation

by

MICHELLE L. WARTER

Submitted to the Office of Graduate and Professional Studies of
Texas A&M University
in partial fulfillment of the requirements for the degree of

DOCTOR OF PHILOSOPHY

Chair of Committee,	Simon W. North
Committee Members,	Steven E. Wheeler
	David H. Russell
	George R. Welch
Head of Department,	Simon W. North

August 2016

Major Subject: Chemistry

Copyright 2016 Michelle L. Warter

ABSTRACT

The dissociation dynamics of ozone photolysis in the Hartley band have been studied to help uncover the origin of the rotational population alternation. Velocity map ion imaging experiments have been performed on the dissociation of ozone at 248, 266 and 282 nm. Rotational distributions and vector correlations for the O_2 (a $^1\Delta_g$) fragment have been measured to elucidate the origin of the observed even/odd J state population alternation. The population alternation is considerably stronger for jet-cooled ozone than the previous measurements at 300 K. The alternation is dependent on J state, i.e., it is weaker at the high and low sides of the rotational distribution, but the alternation is not greatly dependent on photolysis wavelength or O_2 vibrational state. A simple curve crossing model has been used to explain the alternation. The difference in temperature between the previous and current experiments has led to the study of the parent internal energy effects on the alternation. The even/odd alternation is clearly present for a 60 ±10 K beam, but is not observed when the beam temperature reaches 200 ±20 K. This is direct evidence that the parent internal energy must be taken into account to explain the origin of the alternation and is inconsistent with a simple curve crossing model.

The dissociation dynamics have also been studied to help determine if the odd and even J states arise from different dissociation pathways. The correlation between

fragment velocity and rotational angular momentum, the v-J correlation, has been obtained, and no difference in the v-J correlation is observed between the even and odd J states. A previous research group has reported differences between the even and odd states for a 140 K beam, and the difference was shown to be dependent on fragment speed. Since no alternation is present for the 60 K beam, this indicates that the alternation of the v-J correlation may also be dependent on parent internal energy. The spatial anisotropy, the μ-v correlation, showed no alternation in both the current and previous results. It has been shown that the odd J state population increases with increasing parent internal energy, so the odd states may preferentially arise from parent molecules with out-of-plane rotational motion. When the internal energy of ozone is increased, the out-of-plane motion becomes more significant and produces more odd states. A consequence of this is that the out-of-plane motion will depolarize the v-J correlation more than the in-plane parent rotation, but it will not affect the μ-v correlation. Therefore, it would be expected that if the odd states are associated with rotationally excited parent molecules, the v-J would be more depolarized compared to the even states, but the spatial anisotropy would be the same for both states.

DEDICATION

This dissertation is dedicated to my parents, Jim and Linda Warter.

ACKNOWLEDGEMENTS

There are many people I would like to thank. Firstly, I would like to thank my advisor, Dr. Simon North. Thank you for pushing me when I had lost motivation, but also for letting me find my own way. Our conversations over coffee have helped me tremendously and thank you for answering the same question numerous times until it finally clicked in my mind. I could not have asked for a better advisor and I could not have finished graduate school without you.

Thank you to my parents for always being there for me and listening to me when I thought I could not finish. Dad, thank you for teaching me to work with my hands and for our Sunday morning talks. Our conversations gave my mind a much-needed break. Mom, thank you for listening to all my frustrations and for always being there when I needed you. I would not be the person I am today without you. To my brother Ryan, your passion for drag racing has reminded me numerous times about my love for science. Thank you for motivating me even when you were not aware you were helping me.

Colin and Wei, thank you for our random discussions in lab while we were collecting data. I pass the ion imaging torch onto you two. Nic and Feng, thank you for making me laugh so often. I have enjoyed sharing an office with you two. Thank you Monica for all the help with the printer and for looking through years of old purchase

orders when I needed a part number. Lisa, you have been such a great friend. Thank you for always being there. I would like to thank Dr. George McBane for his helpful insight on ozone photodissociation. Lastly, thank you to my other friends and family for the encouragement and support.

TABLE OF CONTENTS

Page

LIST OF FIGURES

FIGURE Page

FIGURE Page

FIGURE Page

FIGURE Page

LIST OF TABLES

TABLE Page

CHAPTER I

INTRODUCTION

"To the Philosopher, the Physician, the Meteorologist, and the Chemist, there is perhaps no subject more attractive than that of ozone." –Cornelius Fox (1873)

The history of the discovery and naming of ozone is very interesting. In 1785, Van Marum was conducting experiments involving electrical sparking above water when he noticed an unusual smell and attributed it to electrical reactions from the experiment. He failed to realize he had in fact, created ozone. 50 years later, Christian Friedrich Schönbein noticed the same odor and recognized it as the smell after a bolt of lightning. He was able to isolate the gaseous chemical in 1839 and named it ozone after the Greek word, ozein, meaning "to smell" due to its pungent odor. However, it was not until 1848 that T. Sterry Hunt correctly predicted the chemical formula for ozone.

Ozone, O_3, is one of the most important atmospheric molecules and its photochemistry has been the subject of numerous experimental[1-16] and theoretical[17-28] studies. O_3 is located in the two lowest layers of the atmosphere; the troposphere and the stratosphere. The troposphere is closest to Earth's surface and extends to 10 km. The tropopause separates the troposphere and stratosphere and in this layer, the temperature remains constant with altitude. The stratosphere is much thicker than the troposphere and ends at ~50 km. Depending on location, ozone can either have

beneficial or harmful effects. Tropospheric ozone is harmful because it is a strong oxidizer capable of damaging living systems. Ozone is the main constituent of urban smog and causes lung irritation as well as damages crops, trees, and other vegetation.[29] Conversely, stratospheric ozone serves a beneficial role since it protects life on Earth. The ozone layer absorbs the majority of the solar ultraviolet radiation in the range of 230-290 nm, protecting life from the harmful effects of the radiation. UV radiation in this range damages DNA and prevents plants and plankton from growing. The majority of the atmospheric ozone is found in the ozone layer which is centered at ~25 km and is ~10 km thick (Figure 1).

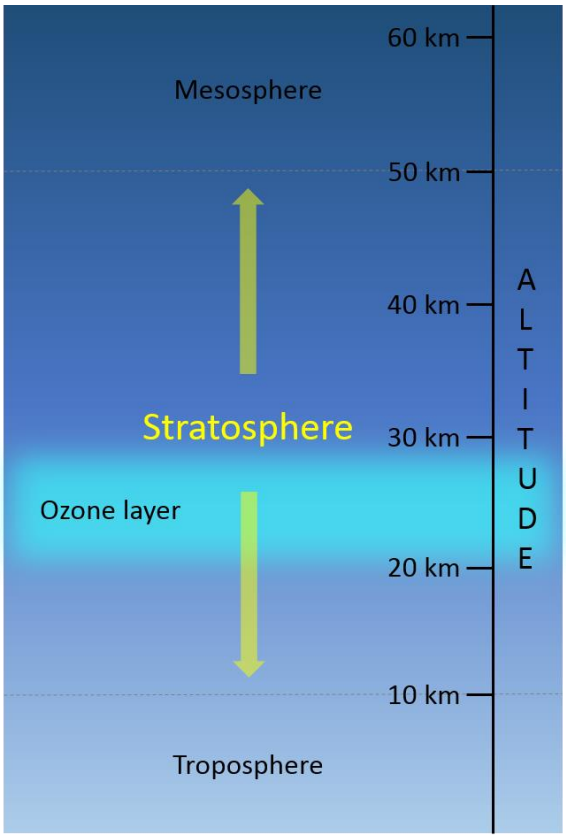

Figure 1: The first three layers of the atmosphere. Ozone is located in the troposphere and stratosphere. The ozone layer is located in the stratosphere and is centered around 25 km.

Figure 2 shows the four regions of the ozone absorption spectrum: the Hartley, Huggins, Chappuis, and Wulf bands along with the solar actinic flux (photons cm^{-2} s^{-1} nm^{-1}) shown with the red dashed line. The green dashed line shows actinic flux at ground level. The absorption cross section is sufficiently large in the Hartley band that all radiation below 290 nm is absorbed. Stratospheric ozone also plays a major role in the temperature of the atmosphere. The temperature of the stratosphere increases from -60°C to 0°C with increasing altitude because O_3 absorbs solar radiation.[30]

Although Ozone plays a very important role in the atmosphere, it is a minor constituent with a concentration ranging from 2 to 8 ppm in the ozone layer and is less than 2 ppm elsewhere.[30]

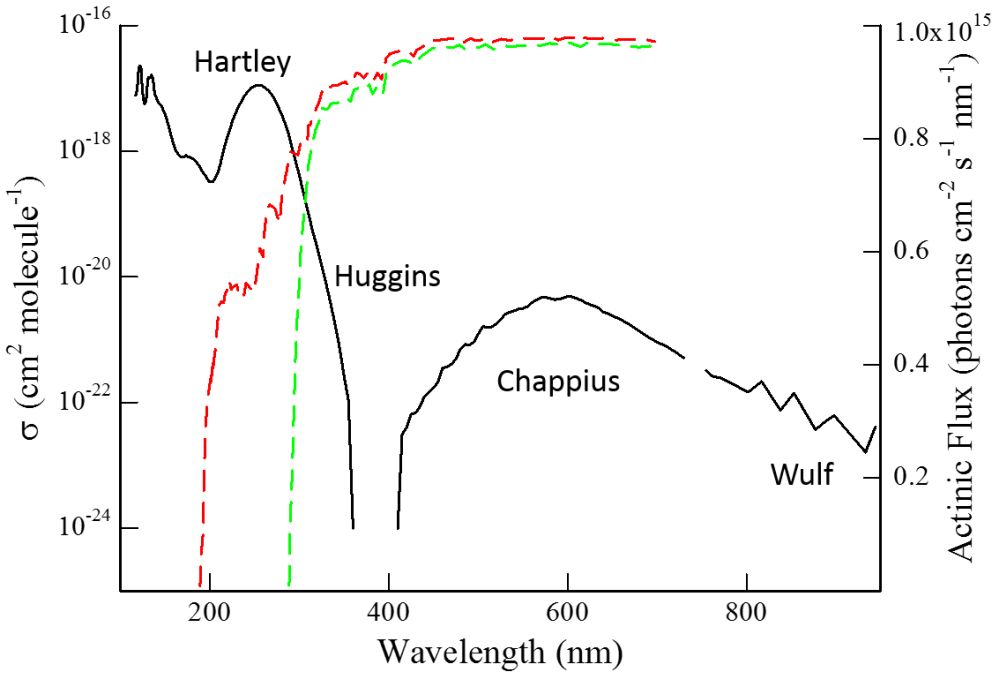

Figure 2: The absorption cross section (solid black line) for O_3, the solar actinic flux before O_3 absorption (dashed red line), and the actinic flux after O_3 absorbs UV radiation (dashed green line)

Ozone depletion has been a growing concern over the past few decades. O_3 concentrations started to decline before 1980 and each year, a dramatic depletion of ozone, referred to as the ozone hole, occurs over the Antarctic. The ozone hole can only be described by a release of halogen-containing molecules by humans.[30] During

each Antarctic winter, the cold temperatures (< -80°C), along with the absence of sunlight, cause polar stratospheric clouds (PSC) to form. The unique chemistry in the PSC facilitates the conversion of chlorine reservoirs into active chlorine which catalytically destroys ozone, creating a dramatic depletion of ozone over the Antarctic in the late winter and spring.[31] Ozone depletion is a major concern because with less ozone in the stratosphere, more UV-B radiation will reach Earth's surface and the risk for skin cancer increases. A 1% depletion of ozone correlates to roughly a 2% increase in UV-B radiation.[30] In 1985, models predicted that the build-up of chlorofluorocarbons (CFCs) will lead to substantial ozone loss and two years later the Montreal Protocol was established which was aimed at reducing the production of ozone depleting substances. It has been found that the concentration of stratospheric ozone started to slowly recover around 2000[32] and based on simulations, should continue to recover in the future.[33] However, concentrations of halogens are expected to be reduced only slightly in the near future so the recovery to the natural levels of halogens is not predicted to occur before 2020.[33]

1.1 Atmospheric Chemistry

In 1930, Chapman was the first to propose a set of oxygen-only reactions which lead to the formation of the ozone layer:

$$O_2 + h\nu \rightarrow O + O \quad (1.1)$$

$$O + O_2 + M \rightarrow O_3 + M \quad (1.2)$$

$$O_3 + h\nu \rightarrow O + O_2 \quad (1.3)$$

$$O + O_3 \rightarrow 2O_2 \quad (1.4)$$

$$[\ O + O + M \rightarrow O_2 + M\ ] \quad (1.5)$$

Reactions 1.1 – 1.5 are referred to as the Chapman cycle, but reaction 1.5 is too slow to play a significant role in stratospheric chemistry. Only 1.1 – 1.4 are usually considered. The Chapman cycle has been used to calculate the absolute concentrations of ozone and when compared to experimental values, overestimates the concentration.[30] In addition to the Chapman cycle, a faster loss process for ozone is needed to account for the overestimation. The concentration of all trace species is too low for there to be any appreciable loss of ozone in the stratosphere, but catalytic cycles can provide a mechanism for significant loss of ozone. The catalytic destruction of ozone is described by the following reactions:

$$X + O_3 \rightarrow XO + O_2 \quad (1.6)$$

$$\underline{XO + O \rightarrow X + O_2} \quad (1.7)$$

$$\text{Net: } O + O_3 \rightarrow O_2 + O_2 \quad (1.8)$$

where X is a reactive species, usually H, OH, NO, Cl, or Br. Reactions 1.1 – 1.4 and 1.6 – 1.7 are the two major cycles that establish the ozone balance in the stratosphere.

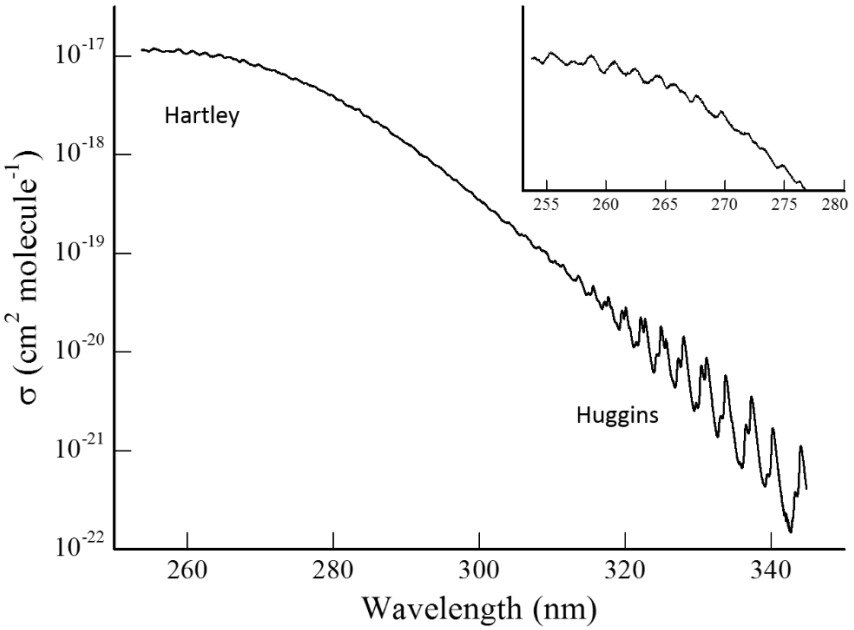

Figure 3: Absorption cross section in the range of 250 – 345 nm corresponding to the Hartley and Huggins bands. Structure is clearly visible in the Huggins band. The insert shows the weaker structure in the Hartley band.

Figure 3 shows the absorption cross section in the range of 250 – 345 nm corresponding to the Hartley and Huggins band. The structure at the top of the Hartley band and in the Huggins band is clearly visible. The Huggins band structure is due to vibronic transitions for excitation from the ground state to the B state. Excitation in the Huggins band corresponds to a bound – bound transition because the energy of the photon lies below the B state dissociation threshold. The structure in the Hartley band cannot be due to vibronic transitions since excitation involves a bound – unbound transition. However, during dissociation, motion in the bending mode provides finite

interferences and these Feschbach type resonances are now known to be the cause the structure in the Harley band.[20, 25]

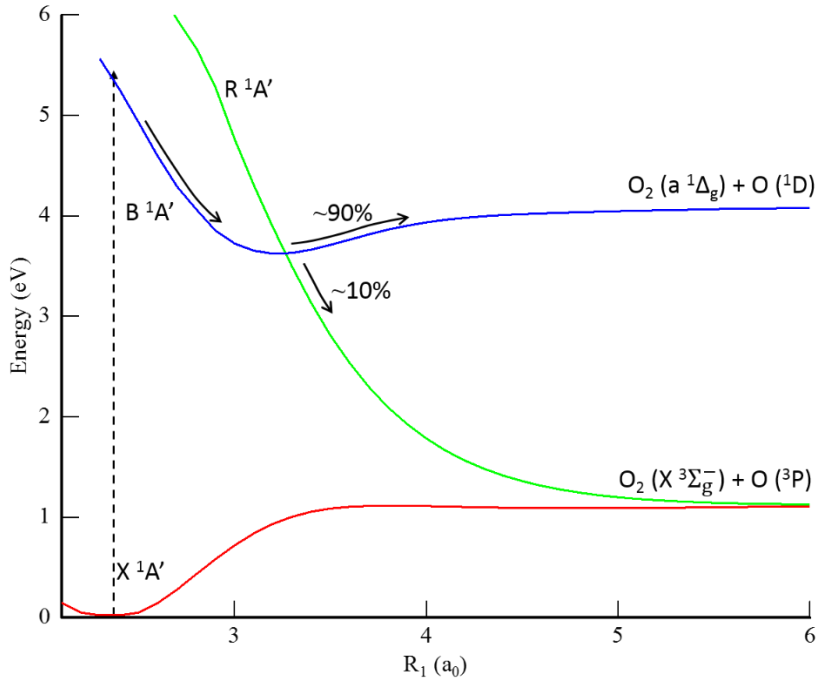

Figure 4: 2-D potential energy surfaces for the X (red), B (blue), and R (green) states at a bond angle of 120°. Approximately 10% of the products cross to the R state and exit through the ground state channel.

Dissociation in the Hartley band coincides with excitation from the X (^{1}A') state to the B (3 ^{1}A') state and produces two, spin-allowed product channels (Figure 4):

$$O_3 + h\nu \rightarrow O_2\ (a\ ^1\Delta_g) + O\ (^1D) \quad (1.9)$$

$$\rightarrow O_2\ (X\ ^3\Sigma_g^-) + O\ (^3P) \quad (1.10)$$

Channel 1.9, the singlet channel, is the dominant channel with a quantum yield of ~90%. This channel is of great interest since the O (^{1}D) fragment is highly reactive and goes on to react with water and produce OH, the "cleanser" of the atmosphere.[30] Absolute O (^{1}D) quantum yields are important for atmospheric modeling. Numerous studies[15, 25, 34-39] have focused on obtaining the O (^{1}D) quantum yield which is shown in Figure 5 for a wavelength range of 220 – 320 nm.

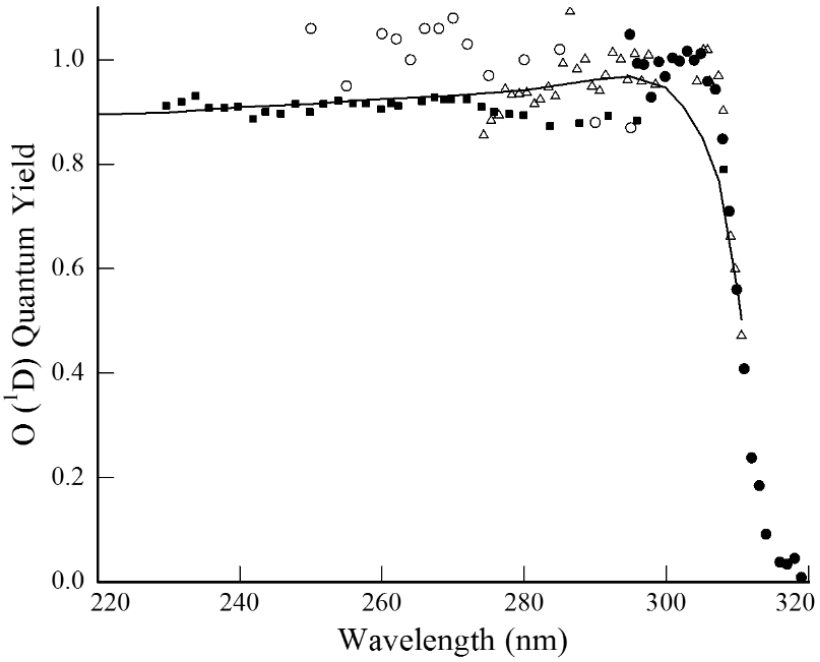

Figure 5: Wavelength dependence of the O (^{1}D) quantum yield from the photolysis of ozone between 220 – 320 nm. Values originally reported by Schinke and McBane (ref. 25) (solid line), Arnold *et al.* (ref. 34) (filled circles), Fairchild and Lee (ref. 36) (open circles), Takahashi *et al.* (ref. 38) (filled squares), and Trolier and Wiesenfeld (ref. 39) (open triangles).

The quantum yield increases sharply around 318 nm, reaches a maximum near unity at 305 nm, then decreases slightly to 0.9. The triplet channel, 1.10, is the minor channel with a quantum yield of ~10% which is independent of wavelength between 266 and 311 nm.[13]

1.2 Ozone Dissociation

Excitation in the Hartley band leads to a transition from the X ^{1}A' state to 3 ^{1}A' (B state). A repulsive potential (R state), which also has ^{1}A' symmetry, crosses through the well of the B state and leads to the triplet channel. The B/R crossing is the only pathway to produce ground state fragments. There is another state with ^{1}A' symmetry (A state), but it has been found to play a minor role in the photochemistry since direct excitation to the A state is very weak and considered negligible.[22] There are a number of crossings between the A, B, and R states, but only the B/R crossing is important in the UV photodissociation of O_3.[25] Therefore, the photodissociation dynamics are dominated by excitation to the B state and either dissociation on the B state to produce excited state products or crossing to the R state to produce ground state products. Figure 6 shows 2-D cuts through the potential energy surface for the B and R states. The green line is the B/R seam and the blue dot is the Franck-Condon point. The B state has two minima depending on which O-O bond is elongated. The R state crosses near the bottom of both minima.

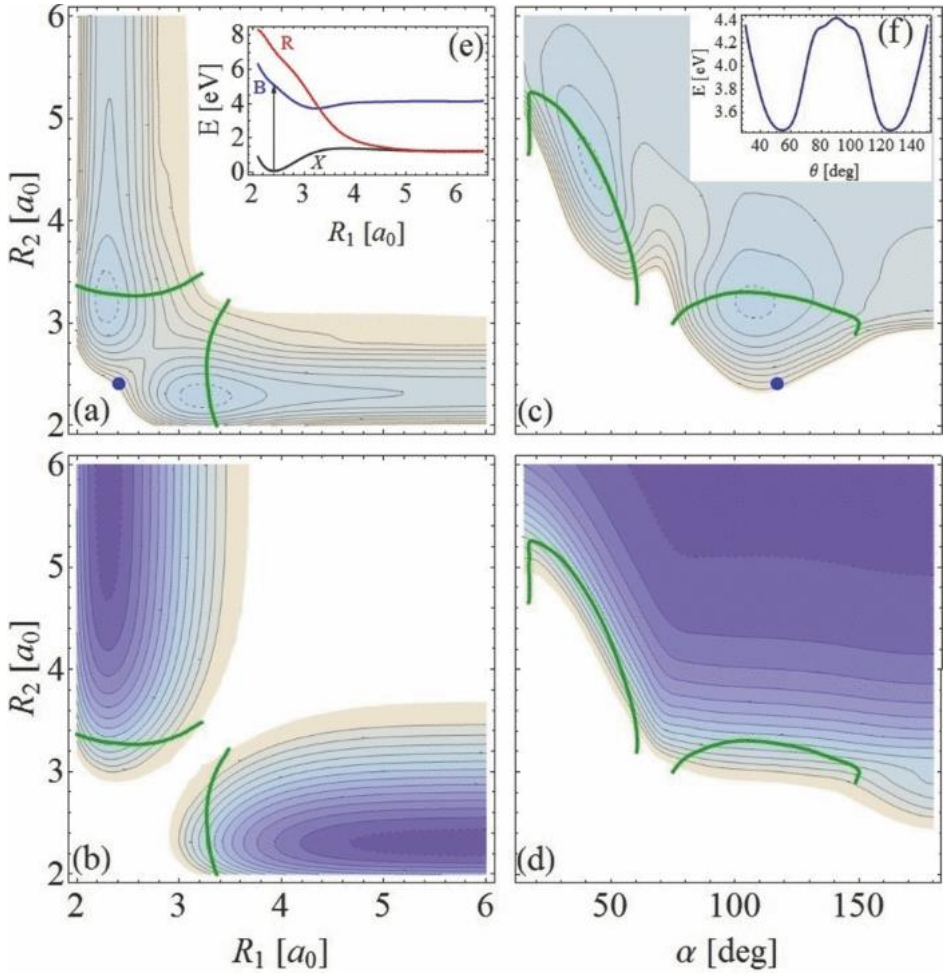

Figure 6: (a)-(d) Two-dimensional cuts through the PESs of the electronic states B [(a) and (c)] and R [(b) and (d)] in the plane (R 1, R 2) of the two O−O bonds [(a) and (b)] and (R 1, α) [(c) and (d)]. The bond angle is fixed at the FC value of α = 117° in (a) and (b); the bond distance is fixed at R 1 = 2.42 a 0 in (c) and (d). The energy of the dashed contour/the contour spacing are 3.6 eV/0.2 eV in panels [(a) and (c)] and 1.2 eV/0.3 eV in panels [(b) and (d)]. Green lines indicate the crossing seam between the diabatic B and R states. Blue dot in (a) and (c) marks the FC point. (e) A cut through the PESs of three electronic states X, B, and R along one O−O bond; R 2 = 2.42 a 0 and α = 117°. (f) A cut through the B state PES along the Jacobi angle θ; the other two Jacobi distances are fixed close to the minimum energy along the B/R CI, at R = 3.8 a 0 and r = 2.3 a 0. Reprinted with permission from Ref. 49.

The transition dipole moment, μ, lies parallel to the line connecting the two end atoms. The B ← X transition is a parallel transition meaning μ must be aligned parallel to the electric field of the laser for the transition to occur. The ground state equilibrium bond angle is 116.8°[2, 17, 20, 40] and the impulse of the dissociation is along the breaking O-O bond. The bond angle initially decreases during the dissociation to the B state equilibrium bond angle of 107°,[22, 23] but at long O-O bond lengths, the bending potential of the B state influences the trajectories, causing them to move towards a more linear configuration.[22] This effect is more substantial for fragments with lower kinetic energy because they will be affected by the bending potential more than fragments with higher kinetic energy.

1.3 Previous Studies

Along with studies to determine the singlet/triplet branching ratio, there have been experiments performed to understand the scalar and vector properties of the ground and excited state channels. Fairchild *et al.*[16] was the first to obtain a translational energy distribution following ozone photolysis at 274 nm. The distribution is not vibrationally resolved, but did provide branching ratios for the two channels. Two years later, Sparks *et al.*[8] obtained a vibrationally resolved translational energy distribution which not only confirmed the work done by Fairchild, but also provided vibrational populations for the first four vibrational states of the O_2 (a $^1\Delta_g$) fragment. Although not rotationally resolved, the widths of the vibrational peaks provides insight

into the width of the rotational distributions. It appears that the distributions become narrower with increasing v state. In 2001, Dylewski and co-workers[2] studied the excited state channel using velocity map ion imaging from O_3 photodissociation at wavelengths in the range of 235 – 305 nm. Vibrational populations, spatial anisotropies, and the orientation of the O (^{1}D) fragment were obtained for every wavelength. It was found that the excitation of ozone was a parallel transition and there was a significant amount of bending during dissociation as discussed in Section 1.2. All the experimental vibrational distributions agree well. They are peaked at v = 0 and decreasing monotonically with increasing v state. A summary of experimentally obtained vibrational populations are shown in Table 1.

Table 1: Vibrational populations for O_2 (a $^1\Delta_g$) from the photolysis of ozone between 240 – 293 nm.

λ (nm)	v = 0	v = 1	v = 2	v = 3	v = 4	v = 5	v = 6	Source
240	64%	15%	8%	4%	5%	4%	2%	Ref. 13
245	34%	23%	20%	8%	8%	4%	0%	Ref. 2
248	49%	15%	15%	8%	8%	5%		Ref. 12
248	65%	18%	8%	5%	3%	4%		Ref. 13
266	52%	27%	14%	7%				Ref. 2
266	57%	24%	12%	7%				Ref. 8
280	70%	30%						Ref. 12
293	76%	24%						Ref. 13

Vibrational distributions have been obtained numerous times, but to date, rotational distributions have only been reported by Valentini *et al.*[13] at 240, 266, and 293 nm. Coherent anti-stokes raman spectroscopy (CARS) spectra of O_2 (a $^1\Delta_g$) were collected following the photolysis of a 300 K ozone sample and the rotational populations were extracted. The distributions show an interesting feature that is not yet fully understood. There is an intensity alternation between the even and odd J states where the population of the even states is greater than the odd states. The origin of the alternation is still unknown, but two explanations have been proposed to explain the origin of the observed population alternation. Valentini and co-workers[13] explained the alternation by attributing it is a selective depletion of the odd states. In the ground state of O_2, only odd J states are allowed due to symmetry constraints. Since O_2 is a homonuclear diatomic, the overall wavefunction should remain unchanged with the exchange of the two nuclei. Odd J states satisfy this requirement and are allowed in the ground state while even J states are not allowed. As a consequence of this restriction, only odd J states can cross from the B state to the R state, leading to a depletion of the odd states in the O_2 (a $^1\Delta_g$) rotational distribution. Baloïtcha and Balint-Kurti[17] have provided an alternative explanation of the alternation stating that the initial wavefunction of ozone and the dissociative wavefunction of the molecule in its electronically excited state must be taken into account. For an ozone molecule with zero total angular momentum, only even J states would be allowed in the O_2 (a $^1\Delta_g$) rotational distribution. When the total angular momentum is increased, the symmetry

restrictions are loosened and the odd J state population will increase. The propensity for even states also explains the population alternation, but it is not clear which explanation is correct. Ion imaging experiments have been performed on jet-cooled ozone to help elucidate the origin of the alternation.

Chapter II describes the experimental apparatus and image analysis. Chapter III goes through the O_2 quantum state distributions with a focus on the intensity alternation in the rotational distributions. Chapter IV focuses on the vector properties of ozone photodissociation and chapter V provides conclusions along with future directions.

CHAPTER II

THE EXPERIMENTAL APPARATUS AND IMAGE ANALYSIS

The experiments described in this thesis employ the technique of velocity map ion imaging (VELMI). The technique captures a 2-D image that can be analyzed to extract both radial and angular distributions of a quantum state-selected photofragment. Due to the conservation of energy and momentum, the VELMI experiment also yields coincident information on the unobserved fragment; the velocity of the detected fragment reveals the internal energy of the co-fragment. This is a very powerful aspect of the experiment which makes it a great choice to study photodissociation. One of the most important requirements is the experiments must be performed in a collision-free environment. To ensure the absence of collisions, the experiments are conducted in an apparatus which is maintained at high vacuum.

This chapter first describes the experimental set-up including a discussion of the photolysis, ionization, and detection techniques. This second part of the chapter discusses beam temperature calibration, how images are analyzed, and the important information obtained after analysis.

2.1 The Experimental Set-up

The VELMI apparatus consists of 3 stainless steel regions: the source, main, and detector chambers as shown in Figure 7. The source chamber is pumped by a 6" Varian 0184 diffusion pump and backed by Welch 1397 belt-driven mechanical pump.

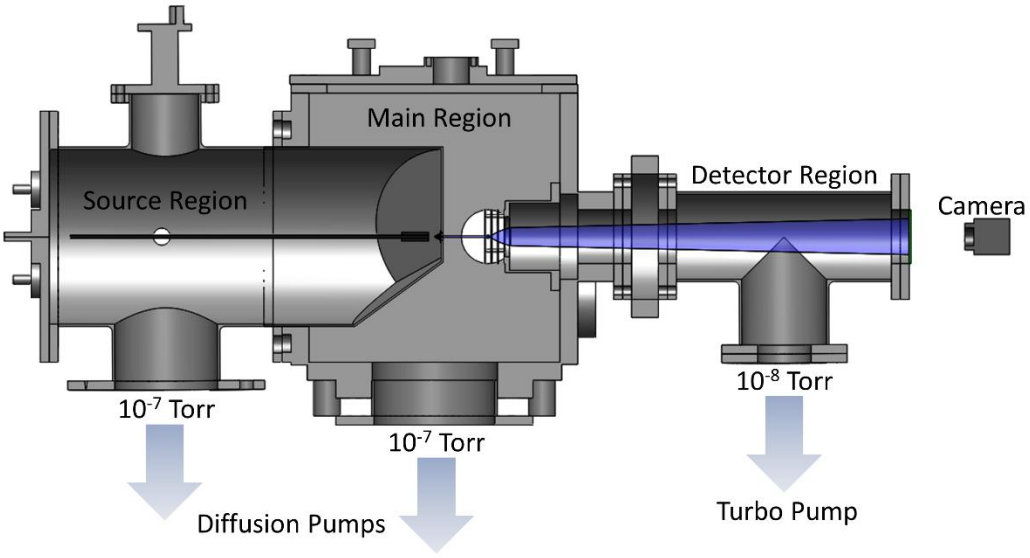

Figure 7: Diagram of the experimental apparatus

The chamber reaches pressures of ~10^{-7} Torr without the pulsed molecular beam. Ozone is generated by flowing O_2 through a CD Laboratory ozone generator and was trapped on silica gel beads in a bubbler at -78°C. During experiments, the bubbler was maintained at ~ -55°C corresponding to an ozone vapor pressure of ~25 Torr. The backing pressure was 800-1000 Torr of helium which flowed through the bubbler to create a 3% O_3 in He beam. The gas mixture flowed through ¼" Teflon tubes to the

solenoid pulse valve inside the source chamber. The pulse valve assembly is shown in Figure 8 shows the aluminum front cap that ensured the beam does not exit at an angle. The beam supersonically expands with a $\cos^2(\theta)$ angular distribution when the pulse valve opens.

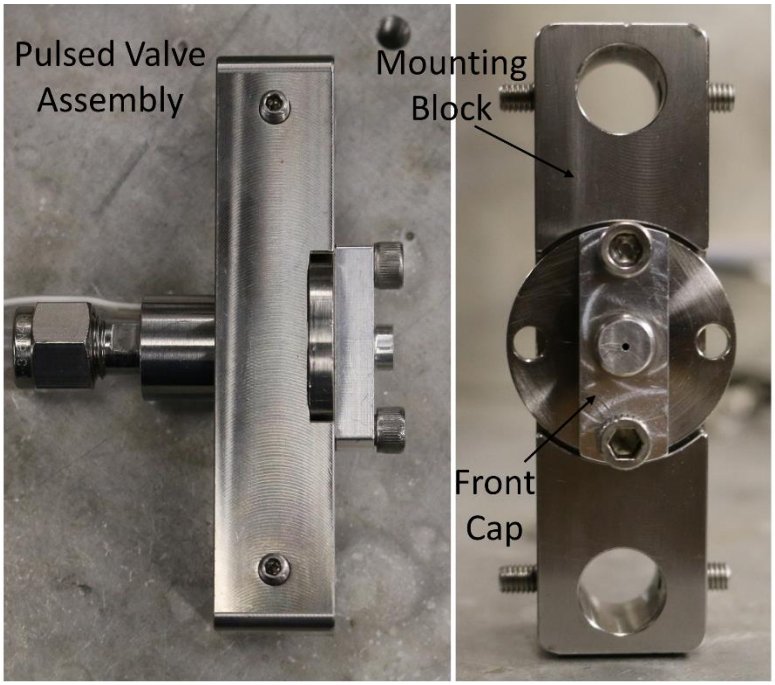

Figure 8: The pulse valve assembly. The front cap was attached to the front of the pulse valve cap to ensure the beam expanded straight.

Typically, the pulse valve was opened for 800 μs. Only molecules that have velocity in the z-axis (TOF axis) with an angular distribution width of 4.5° ± 0.5° will pass through the stainless steel, conical skimmer into the main chamber. It is vital that the parent molecules have small initial velocity in the x, y plane. When detecting the fragments,

any velocity deviation from the center of the image is attributed to the recoil velocity imparted on the fragments from the dissociation. Parent molecules possessing velocity in the x, y plane, can significantly lower the resolution of the recoil velocity determined.

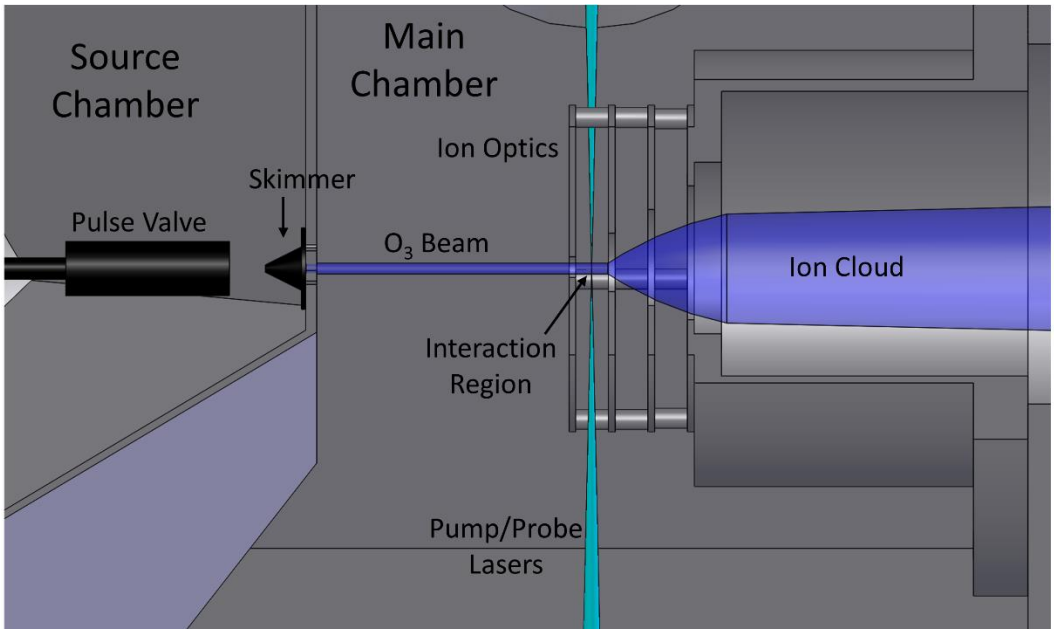

Figure 9: Diagram of the inside of the source and main chamber. Once the O_3 beam travels through the skimmer, it reaches the interaction region where it will be photolyzed and the fragments will be ionized. The ion cloud is accelerated by the ion optics.

Similar to the source chamber, the main chamber is pumped by a 6" Varian 0184 diffusion pump, backed by Welch 1397 belt-driven mechanical pump and also reaches pressures of ~10^{-7} Torr without the pulsed molecular beam. The parent molecules reach the interaction region where they will be photolyzed. The laser beams

cross the molecular beam at 90° where ion optics accelerate the ions toward the detector region. The inside of the source and main chamber are shown in detail in Figure 9.

The detector region is pumped at all times by an oil-less Turbovac 151 turbo molecular pump and backed by an Edwards 30 direct drive mechanical pump. The turbo molecular pump allows the detector region to reach pressures of $\sim 10^{-8}$ Torr. At the end of the detector region, there is a position-sensitive detector that consists of two microchannel plates (MCP) and a phosphor screen. A charge-coupled device (CCD) camera behind the phosphor screen captured the image on the back of the phosphor screen every laser shot and transferred it to the computer. Images were accumulated for 1,000-10,000 laser shots.

2.2 Photolysis

O_3 was photolyzed in the Hartley band at 248, 266, and 282 nm to study the dominant O_2 ($a^1\Delta_g$) + O (^{1}D) channel. A GAM EX10/200 excimer laser with krypton fluoride gas was used to generate 248 nm. The 266 nm beam was obtained by the 2nd harmonic of the 532 nm output of a Big Sky Ultra laser. The output of a Nd:YAG laser (532 nm) pumped a Quanta - Ray PDL - 1 dye laser (Rhodamine 590 dye) and the dye output was doubled to produce 282 nm using a Spectra-Physics wavelength extender (WEX). All lasers had a pulse frequency of 10 Hz and temporal width of 10 ns. Laser

powers used were approximately 650 μJ/p, 1.2 and 2 mJ/p for 248, 266, and 282 nm respectively. To obtain images at all four laser geometries, the polarization of the lasers had to be controlled. The excimer laser produced unpolarized light, so it was polarized using a pile-of-plates polarizer. To switch the polarization, the pile-of-plates was rotated 90°. The 266 and 282 nm lasers were linearly polarized and a double Fresnel rhomb was used to rotate the polarizations. The lasers were ~93% polarized. A Glan-Taylor polarizer was used to check laser polarizations and to ensure the complete polarization of the laser if necessary. The photodissociation laser crossed the molecular beam at 90° and O_3 absorbs one UV photon and dissociated about 40 fs[1, 20] later to produce excited state fragments. On average, 77% of ozone molecules dissociated. When the parent molecule dissociates, a recoil velocity is imparted on both fragments and they travel away from each other with equal momentum. The velocity of each fragment is based on the mass partitioning factor which will be discussed later in Section 2.7. Due to the short excited state lifetime, fragment velocities have a preferential direction related to the transition dipole moment.

2.3 Ionization

Once ozone is photolyzed, the O_2 (a $^1\Delta_g$) photofragments can be detected. For velocity map ion imaging, it is important to state-selectively probe the fragments so the internal energy is known exactly. Resonant enhanced multi-photon ionization (REMPI) is a useful state-selective spectroscopic technique that is frequently used for state-

selected ionization. REMPI involves excitation to a resonant state followed by ionization of the fragment. The total number of photons needed varies depending on the fragment and the energy of the resonant state and is written as (m + n) REMPI where m is the number of photons for excitation to the resonant state and n is the number needed for ionization. (2 + 1) REMPI was used to probe O_2 ($a^1\Delta_g$). For the ionization step, it is assumed that since the mass of the ejected electron is much smaller than the mass of O_2, the velocity of the fragment is not significantly affected. The newly created ion can be detected with high efficiency. An example REMPI spectrum is shown in Figure 10 for CO arising from the 230 nm photolysis of OCS.

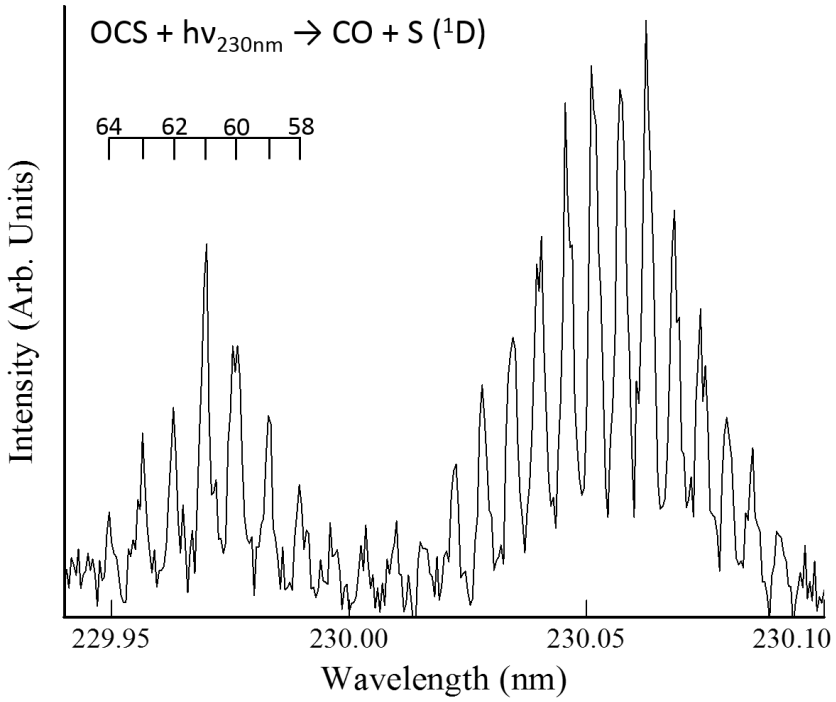

Figure 10: (2 + 1) REMPI of CO from the 230 nm dissociation of OCS.

The resonant state that was used for probing O_2 was the d $^1\Pi_g$ state which is a low-lying Rydberg state and interacts with the nearby II $^1\Pi_g$ valance state.[41-43] The interaction causes the d (v' = 1-3) states to predissociate to the O (^{3}P) + O (^{3}P) channel which produces a perturbation in the rotational spectra. The v' = 0 of the d state does not appear to be significantly perturbed. The vibrational energies are not significantly shifted and the anomalous intensities observed are due to J-dependent resonances in the ionization step.[41] Although REMPI via these states has been used previously in the study of ozone[3-5], using these states does not provide accurate rotational populations. Vibrational states, v' ≥ 4 are above the dissociation threshold for the II $^1\Pi_g$ state and do not show any effects of perturbation in the rotational distributions. Therefore, given our interest in rotational populations, we decided to exploit excitation to v' = 4. The O_2 REMPI scheme is shown in Figure 11.

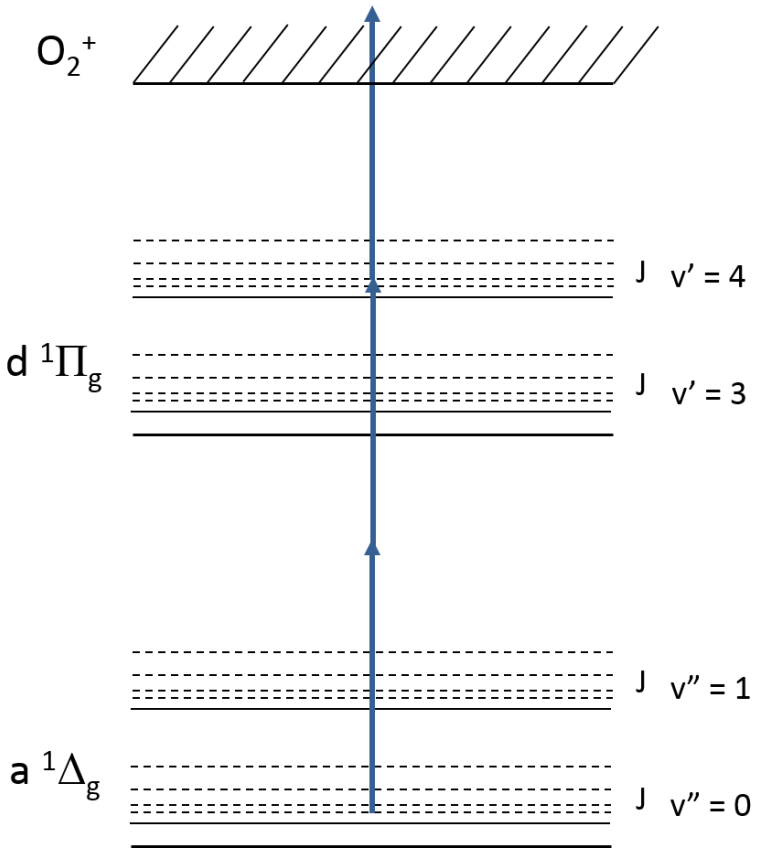

Figure 11: Schematic (2 + 1) REMPI scheme for probing O_2 ($a^1\Delta_g$)

Table 2: Constants for the ($a\ ^1\Delta g$) and ($d\ ^1\Pi$) states of O_2.

	T_e (cm^{-1})	B_e (cm^{-1})	D_e (cm^{-1})
O_2 ($a^1\Delta_g$) v = 0	7918.1	1.4114	4.86×10^{-6}
O_2 ($a^1\Delta_g$) v = 1	-	1.4008	4.86×10^{-6}
O_2 ($d^1\Pi_g$) v = 4	73746.87	1.5883	4.56×10^{-6}

After the scans were collected, they were fit with a simulation calculated using the constants in Table 2. Accurate constants were determined by performing a non-linear least squares fit to equation 2.1 using the term values from Morrill *et al*.[41] The term values and fits for v = 0, 1 of the a state are shown in Figure 12. After the scans were fit, the rotational populations were extracted.

$$Term\ Value\ (J) = D_e + B_eJ(J+1) - D_eJ^2(J+1)^2 \qquad (2.1)$$

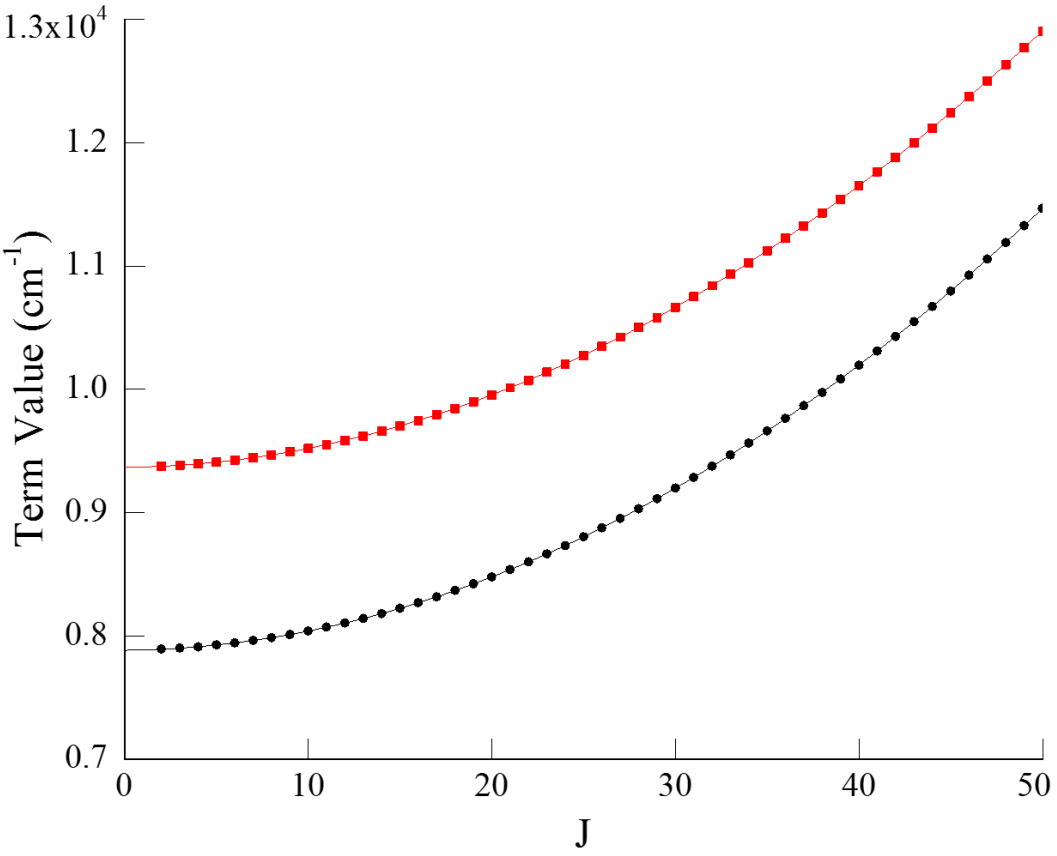

Figure 12: Term value vs. J for O_2 ($a^1\Delta_g$, v = 0, 1). The black circles are the v = 0 data and the red squares are the v = 1 data. Both are fit with a non-linear least squares fit.

Rotational distributions for O_2 ($a^1\Delta_g$, v" = 0, 1) were collected via excitation to the O_2 ($d^1\Pi_g$, v' = 4) state. The transitions for v" = 0 and v" = 1 required 304 and 310 nm respectively. The wavelengths were obtained by pumping a tunable LAS dye laser with the 2nd harmonic of a Nd:YAG laser (532 nm). The output of the dye laser was then doubled to reach the required wavelength. A mix of Rhodamine 610 and Rhodamine 640 laser dye was used for both wavelengths. The ratio of 610:640 was 20:1 for 304 nm and 5:1 for 310 nm for the oscillator cell and diluted, as needed, for the amplifier cell. All probe wavelengths were 99% polarized and the power required for both transitions was in the range of 2-4 mJ/p. Images of O_2 ($a^1\Delta_g$, v = 0, j") were collected via excitation to v' = 2 of the d state. The population alternation, which will be discussed later, was weaker for this transition, so the signal-to-noise was sufficient for the odd states to collect images for the four laser geometries. The wavelength needed for the v' = 2 ← v" = 0 transition was 320 nm. The same laser set-up, with DCM laser dye was used. The power used was about 3 mJ/p.

2.4 Detection

Once the ions are created in the interaction region, they are accelerated and focused by a set of ion optics. The first lens, the repellor, has the largest applied voltage. This lens accelerates the ions down the time of flight tube after they have been

created via the REMPI process. The following lenses focus the velocity of the ions so the radial displacement on the image is only attributed to the x, y velocity component of the fragment due to dissociation, and not influenced by initial position. The ion optics can also stretch or compress the temporal profile of the ion cloud. SIMION trajectories[44] are shown in Figure 14 for 4000/2988 V for the repellor and lens 1 respectively. SIMION is used to determine the ion optics voltages that provide the best velocity focusing.

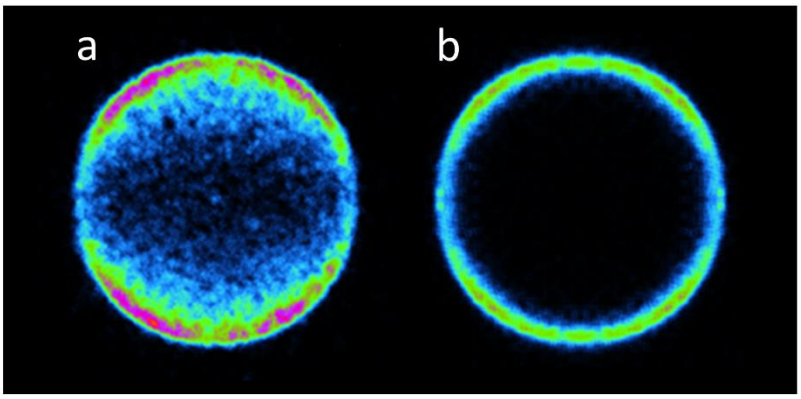

Figure 13: NO (X, v = 0, N = 26.5) images from the 355 nm dissociation of NO_2. Both the dissociation and probe lasers are polarized parallel to the imaging plane. a) Crushed ion image b) sliced ion image

The entire ion cloud can be collected (crushed imaging) which results in the cloud being 'crushed' on the detector and a 2-D image of the 3-D cloud is obtained. Alternatively, the cloud can be stretched and the detector gated so only a small, central slice of the cloud is detected (sliced imaging). Figure 13 shows a crushed and sliced NO image from

the 355 nm dissociation of NO_2 to illustrate the difference between the two methods. In the crushed image, there is signal towards the center of the image. This is the z-axis velocity component to the one ring in the image. If there was another ring with a smaller radius, the higher velocity signal would contribute to the lower velocity signal. The sliced image by contrast, does not have any signal towards the center of the image because by only detecting a thin central slice, the z-axis velocity component is not detected. The detector width was ~300 ns for crushed images and ~40 ns for sliced. The advantages and disadvantages of crushed and sliced imaging will be discussed in Section 2.6.

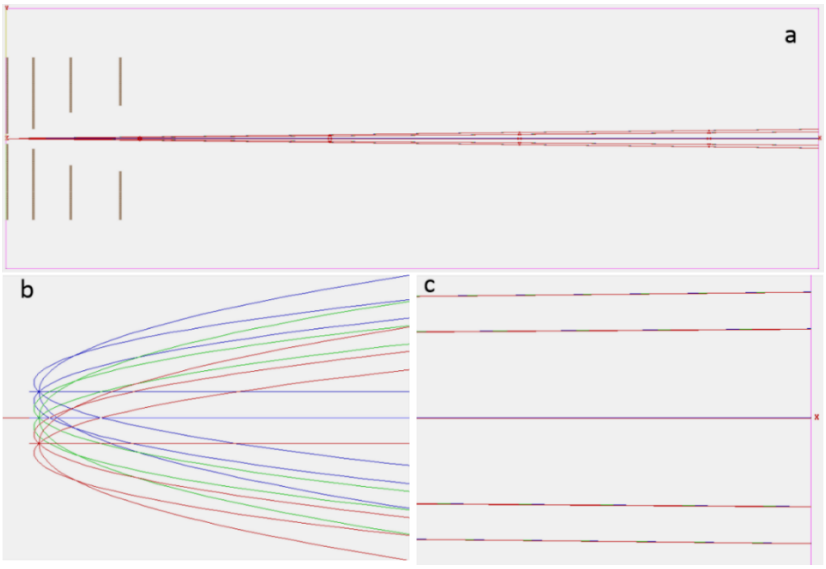

Figure 14: SIMION trajectories for ion optic voltages a) full ion trajectories for 4000/2988 V b) ion trajectories in the interaction region c) ion trajectory in the region of the detector. The velocities have been focused by the ion optics so the ions with the same velocity, regardless of initial position, will hit the detector at the same radius.

After ionization, the ions travel down the field-free TOF tube where they hit a position sensitive detector (Figure 15). The detector consist of two MCPs in a chevron configuration with a phosphor screen directly behind them. The ions hit the front, grounded MCP and the impact ejects electrons through the channel creating a cascade of electrons (> $x10^6$ gain). The position where the electrons hit will illuminate and can be detected by the CCD camera. The detector is gated to only detect fragments based on their mass-to-charge ratio (O_2^+ m/z = 32) which decreases the background signal collected. The back voltage of the MCP must exceed 1.6 kV for any appreciable gain to occur. The arrival time of the fragments also depends on the voltages of the ion optics and once the arrival time for a given mass is determined, the voltage is increased to 2.2-2.4 kV. At all other times, the voltage is at 1.6 kV so minimal signal is detected.

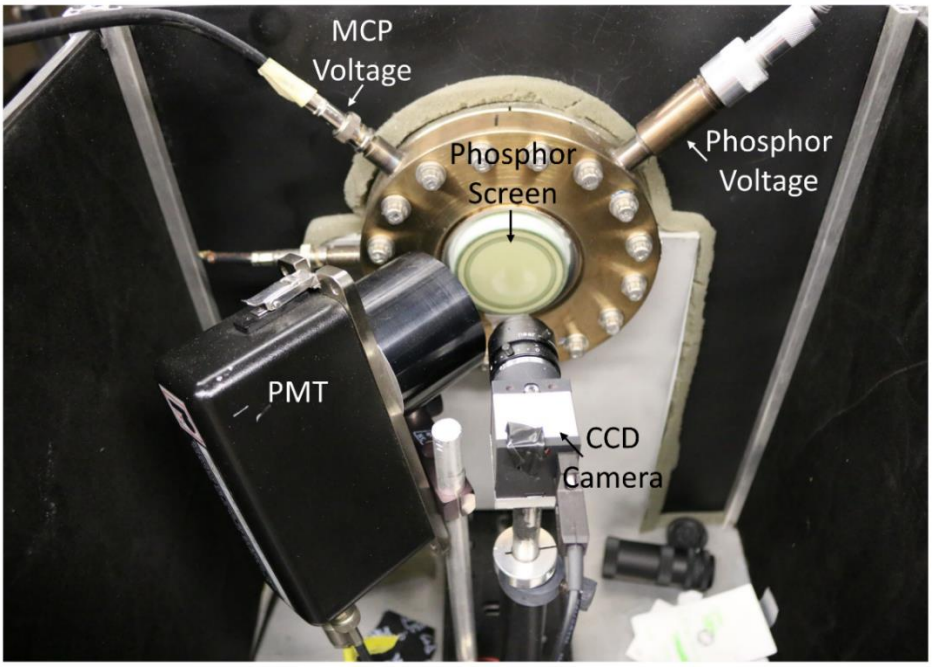

Figure 15: Picture of the back of the detector showing the back of the phosphor screen, PMT, and camera.

There are two modes of detection for the VELMI experiment. A photomultiplier tube (PMT) can be used to collect the overall ion signal. This is used when the rotational spectra are desired since spatial information is not necessary. During these experiments, there was some signal from the probe laser dissociation in the center of the image. To obtain better O_2 scans, an optical block was made and attached to the back of the phosphor screen to reduce the signal at the center of the image as the probe laser was scanned. For other experiments, a block was also made for any background at larger radii than the O_2 ring. A charge-coupled device (CCD) camera is used to collect ion images. The camera records the position of the photons emitted

from the phosphor screen which provides spatial resolution. The output of the camera is a 768 x 768 2-D array. An array is collected for each laser shot and added to the previous arrays. This is continued until the signal-to-noise is sufficient.

2.5 Molecular Beam Temperature Calibration

To characterize the rotational temperature of the molecular beam, a beam of NO in He was used and the NO was probed using (1 + 1) REMPI via the A ← X transition at 226 nm. The rotational spectrum of NO was collected and fit with a simulation to determine the temperature of the beam. It is imperative that the same part of the expansion is probed for both the NO and the O_3 beams since different parts of the expansion will have different temperatures. The velocity of the beam relies on the average mass, so the percent of molecules seeded in He needed to have the same average mass of the O_3 beam. The beam of O_3 was 3% which required a NO/He beam of 5%. The gas mixture was made using a high pressure mixing station and high pressure tank. During experiments, the tank was connected to the pulse valve and the flow was set to 800-1000 Torr. The 2^{nd} harmonic of a 10 Hz Nd:YAG laser was used to pump a tunable Scanmate dye laser with Coumarin 450 dye. The dye output was then doubled to achieve the desired wavelength. For a given pulse valve delay time, the laser was scanned over a small range of wavelengths to ionize NO and the total signal was collected with the PMT to obtain the rotational spectrum. The pulse valve delay was changed and the experiment was repeated. For each scan, the power of the laser was

also collected using a photodiode. To obtain the temperature of the beam, the NO rotational distributions were imported into LIFBase[45] and the temperature of the simulation was adjusted until the best fit was found.

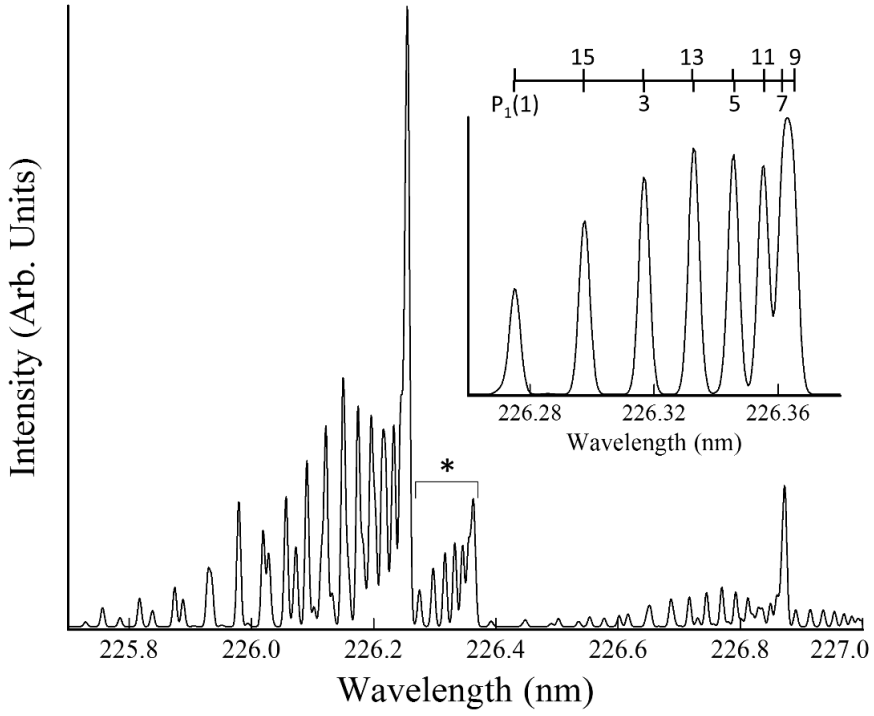

Figure 16: NO A (v' = 0) ← X (v" = 0) simulation. Inset shows the P_1 branch that was probed to determine the temperature of the molecular beam.

Three NO temperature scans were collected and fit using LIFBase. Figure 16 shows the NO v" = 0 simulation. We focused on the P_1 branch, shown in the inset of Figure 16, between 226.26 and 226.38 nm which had seven peaks to fit. The wavelength range was chosen because the P_1 branch is isolated and the lower NO

rotational states produce the greatest population difference at temperatures around 50-100 K. Firstly, all the NO scans were power corrected before fitting. Then they were imported into the simulation program and the resolution of the simulation was set to 0.03. The temperature was adjusted until the best fit was found for each scan. The best fit was determined visually. The temperatures of the scans were 50, 80, and 100 K ± 5 K at the three pulse valve delays. The 80 K spectrum and fit are shown in Figure 17.

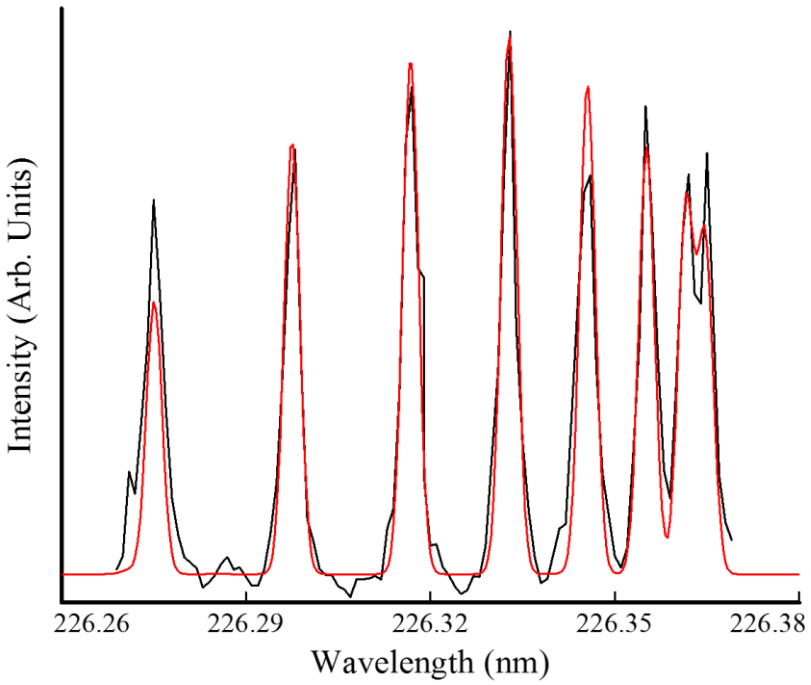

Figure 17: 80 K NO A ← X spectrum of the P_1 branch is shown in black and the fit is shown in red.

2.6 Image Processing

Once we have the raw ion image, we must process it in order to obtain radial and angular information. The first step is to convert from Cartesian to Polar coordinates since I(r,θ) is a more convenient coordinate system because it is more relevant to the physical properties of the dissociation. The center of the image must be found first before the conversion. It is very important to find an accurate center which is not trivial. If the center of the image is off by a few pixels, the radial and angular distributions are blurred and accurate anisotropies and speeds cannot be determined. To find the center, we employ a four-fold symmetrization. Since each quadrant of the image is identical, we can fold them on each other and adjust the (x, y) value for the center until the quadrants overlap. The four-fold symmetrization not only provides the center of the image, but it also increases the signal-to-noise. For a crushed image, the entire 3-D cloud is projected on a 2-D detector, so the radii are not proportional to the fragment's speed because the z-axis velocity component of the faster fragments contaminates the signal of the slower fragments. The 2-D distribution must be reconstructed in order to attain an accurate distribution. The reconstruction method used is the Polar Onion Peeling (POP) algorithm.[46] This straight forward method involves 'peeling' layers of signal from the image one at a time. The signal of the fastest fragments is at the largest radius and does not have any speed contribution in the z-axis. Therefore, the signal attributed to the fastest fragments in the crushed image is identical to the 3-D distribution. This signal is subtracted from the rest of the image.

This creates a new image where signal from the new outer ring can now be subtracted from the image. This is continued until the entire 3-D distribution is retrieved. Figure 18 shows an image throughout the processing method. One requirement of the POP method is the image must contain cylindrical symmetry. This is fulfilled only when both the linearly polarized lasers are polarized parallel to the detection plane. Only one of the four possible laser geometries produces a cylindrically symmetric image. At times, it is necessary to use laser geometries that do not fulfill this requirement so the POP algorithm cannot be used. In these cases, sliced imaging is a preferred experimental method.

Sliced images are a 2-D slice through the center of the ion cloud.[47] Since the 3-D cloud is not crushed, sliced imaging provides an image where the radii of the rings are directly proportional to the speed of the fragment. The image does not require reconstruction, so any combination of laser polarizations can be used. This is useful if vector correlations are of interest because images that break cylindrical symmetry are needed. To collect sliced images, the ion cloud must be stretched temporally by the ion optics. The gate width of the detector is decreased to ~40 ns and the delay is set to capture a thin slice through the center of the cloud. The disadvantage to sliced imaging is only a small fraction of the signal is collected so it is more difficult to get images with good signal-to-noise.

If the image only consists of a single ring, a crushed image can be collected and the image does not have to be reconstructed. This is referred to effective slicing. Since

the outer most ring does not have any contribution from any other signal, it can be treated as though it is a sliced image. This is advantageous because all the signal can be collected so the signal-to-noise is better and all laser geometries can be used.

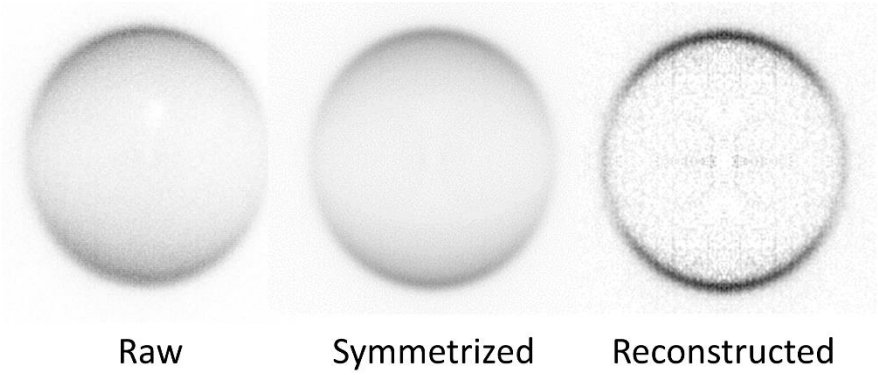

Figure 18: Images throughout the processing method. The collected raw image is first symmetrized. The symmetrization process increases the signal-to-noise and locates the center of the image. The image can then be reconstructed if needed. If not, the symmetrized image is analyzed.

2.7 Information Obtained

Now that the image is processed, it needs to be analyzed to obtain information about the dissociation. Since our experiments produce coincident results, equation 2.2 is used to determine the internal energy of the co-fragment.

$$E_{h\nu} - E_{rxn} + E_{ozone} = E_{avail} = E_{trans} + E_{int}^{O_2} + E_{int}^{O} \quad (2.2)$$

After the parent molecule dissociates, the energy leftover, the available energy, can be divided between the translational energy and the internal energy of both fragments. Since the molecular beam supersonically expands into the chamber, it is assumed that the contribution to the available energy from the parent internal energy is negligible. The translational energy is measured and the internal energy of the O_2 fragment is state-selected, so the internal energy of the co-fragment can be calculated. Multiple rings in an image are due to the probed fragment formed in coincident with multiple states of the co-fragment. For the O_3 experiments discussed in this thesis, the atomic oxygen co-fragment is only produced in one state. Therefore, all the images only have one ring. The information obtained from the images fall into two categories: scalar and vector properties. The disposal of the available energy is a scalar property while angular distributions and vector correlations are vector properties.

2.7.1 Radial Distributions

The radial distributions represent the angle averaged signal at each radius. Since the fragment speed and radius are linearly related, the radial distribution is a direct measure of the speed distribution. If the fragment is formed with a co-fragment in more than one state, the relative peak intensities give information about branching ratios. When the radial distribution is first determined, the radius is given in pixels which is not useful. Pixels need to be converted to fragment speed using a linear factor referred to as the speed-to-pixel ratio. This factor is dependent on the ion optics

voltages and the mass of the probed fragment. If the molecular fragment is probed in a triatomic dissociation, it is trivial to find the conversion factor since the internal energy at the atomic co-fragment is known exactly. The speed-to-pixel for O_2 for ion optics voltages of 4000/2988 V for the repellor and lens 1 respectively was found by fitting the radial distribution in pixels with a simulation. Since the internal energy of the O atom is known, the only unknown is the conversion factor which was adjusted until the simulation fit the experimental data. The speed-to-pixel was found to be 11.49 m/s/pixel. The radial distribution for O_2 (a $^1\Delta_g$, v = 0, J = 33) from the 248 nm photolysis of ozone is shown in Figure 19.

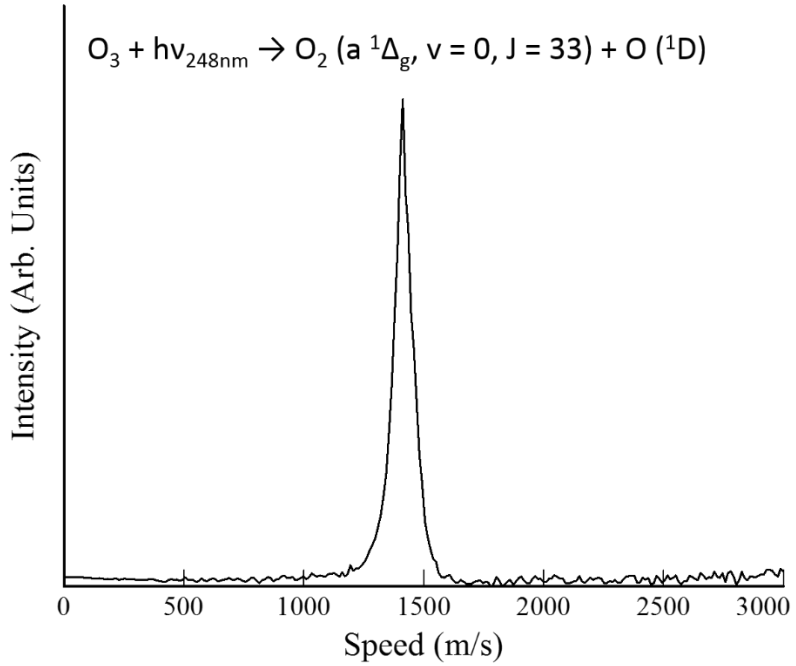

Figure 19: Radial distribution for O_2 ($a^1\Delta_g$, v = 0, J = 33) from the 248 nm photolysis of O_3. The speed-to-pixel used was 11.49 m/s/pixel.

Alternatively, the radial distribution can be expressed in total translational energy. The total translational energy is given by equation 2.3,

$$E_{trans} = \frac{1}{2}\mu v_r^2 \tag{2.3}$$

where μ is the reduced mass and v_r is the relative velocity. Since energy and momentum are conserved, equations 2.4 and 2.5 can be used to relate the translational energy to the fragment velocity (equation 2.6).

$$v_r = v_{O_2} + v_O \tag{2.4}$$

$$m_{O_2} v_{O_2} = m_O v_O \tag{2.5}$$

$$E_{trans} = \frac{1}{2} m_{O_2} \left(\frac{m_{O_2}}{m_O} + 1\right) v_{O_2}^2 \tag{2.6}$$

However, conversion from velocity to translational energy is not linear and a Jacobian factor of $\frac{1}{v_{O_2}}$ is required.[48]

2.7.2 Angular Distributions

Angular distributions describe the signal with respect to the angle around the ring for a given radius. Angular distributions are very helpful for understanding the dynamics of the dissociation and the nature of the dissociative transition. By analyzing the angular distributions, vector correlations can be determined which provide a wealth of knowledge for understanding the underlying dynamics. The origin of an anisotropic angular distribution is due to the effects of two absorption events: the

absorption of the pump photon and the absorption of the resonant photons from probing the fragment. The linearly polarized pump laser aligns the parent molecules in the lab frame by preferentially dissociating molecules that have the transition dipole moment, μ, parallel to the electric field of the laser, E. The probability of a molecule absorbing a photon follows equation 2.7,

$$P = |E \cdot \mu|^2 = (|E||\mu| \cos\theta)^2 \quad (2.7)$$

where θ is the angle between the electric field and the transition dipole moment. Molecules with μ perpendicular to E have zero probability of absorbing a photon while the greatest probability of absorbing a photon is when the vectors are parallel. If the parent molecule dissociates fast relative to a rotational period, the fragments will be ejected with a given anisotropy based on the correlation between μ and the velocity of the fragment, v. Similar to how the μ-v correlation creates an anisotropic distribution of fragments, the linearly polarized probe laser can preferentially ionize the fragments based on the transition branch and the alignment of the angular momentum. This correlation, the μ-J correlation, is referred to as rotational alignment. If the parent molecule has a long dissociative lifetime, the μ-J and μ-v correlations can be lost, but the v-J correlation will still be present. The v-J correlation is solely based on the fragments after dissociation, so the parent lifetime has no effect on the value.

The angular signal intensity is dependent on the number of photons for the dissociation and resonant step of REMPI. Each photon, barring saturation, adds a ($\cos^2$ θ) term to the angular distribution. For the ozone experiments, there was one

dissociation photon and O_2 was probed with two resonant photons. Therefore, we can expect an overall signal intensity with a ($\cos^6\theta$) term (Figure 20). The intensity of the signal can be described by equation 2.8,

$$I(\theta) = \frac{1}{4\pi}[1 + \beta_2^{FG} P_2(cos\,\theta) + \beta_4^{FG} P_4(cos\,\theta) + \beta_6^{FG} P_6(cos\,\theta)] \qquad (2.8)$$

where $P_n(\cos\theta)$ are Legendre polynomials, β_n is referred to as the anisotropy parameter ($-1 \leq \beta \leq 2$), and F and G indicates the lab-frame polarization of the linearly polarized pump and probe lasers respectively. A non-linear least squares fit is used to fit the angular distribution and determine the β_n values.

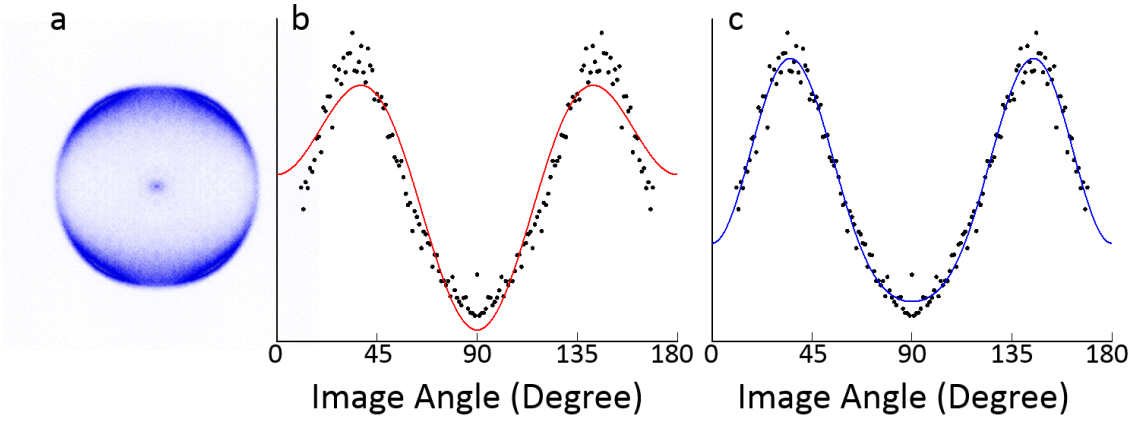

Figure 20: a) VV O_2 (a, v = 0, J = 32) image from the 248 nm dissociation of O_3, b) and c) show fits to the angular distribution for the image. b) Angular distribution fit with a maximum of a ($\cos^4\theta$) term. c) Angular distribution fit with a maximum of a ($\cos^6\theta$) term. The fit with the higher term fits better because it takes into account all three photons for the entire dissociation and ionization process.

CHAPTER III

O_2 ROTATIONAL STATE DISTRIBTUIONS

The rotational distributions of O_2 (a $^1\Delta_g$) have been previously reported by Valentini *et al.*[13] at wavelengths between 230 and 311 nm in a 300 K sample. The distributions are peaked at high J for 240 nm (approximately J = 30) with the maximum shifting to lower J with increasing wavelength. For a single dissociation wavelength, the rotational distribution moves to lower J with increasing vibrational state. The authors also observed that the populations of the odd rotational states were lower relative to the even states. This population alternation is largest for the shortest wavelengths, but diminishes to very small values at wavelengths > 293 nm. There was also a strong vibrational state dependence observed at every wavelength; the difference between odd and even states decreasing with increasing vibrational state. Such an alternation is not observed in O_2 (a $^1\Delta_g$) produced by a microwave discharge, implying that it results from photodissociation dynamics. Valentini *et al.*[13] have proposed that this interesting behavior arises from a depletion of the odd states due to crossing to the R state and dissociation to the triplet channel. The O_2 (X $^3\Sigma_g^-$) products can only have odd J due to nuclear spin statistics and thus only these states can couple to the R state.

Resolved rotational distributions have not been reported in a free jet expansion to examine the influence of initial parent internal energy on the population alternation. This dissertation presents such measurements at 248, 266, and 282 nm revealing

significantly greater even/odd alternation than observed in the 300 K rotational distributions of Valentini.[13] Indicating that parent internal energy plays an important role in this phenomenon. The results are also compared to recent classical[22] and quantum mechanical[49] calculations using updated potential energy surfaces. Both scalar and vector properties have been measured. The current chapter focuses on the rotational properties and the following chapter focuses on the vector properties.

Rotational distributions were collected for O_2 (a $^1\Delta_g$) fragments following the UV photolysis of ozone. All rotational scans were obtained by scanning the probe laser and collecting the overall signal with a PMT. The scans were collected in segments and multiple scans of each segment were averaged together. The scans were baseline corrected, if needed, by choosing 4 – 5 points that were off resonance and fitting them to a line. Then the correction was subtracted from the scan. The probe laser power was collected at multiple wavelengths for each segment and the scan was power corrected using the square of the power since the resonant step of REMPI involved two photons. After baseline and power corrections, the segments were spliced together.

The scans were fit with a simulation using the O_2 (a $^1\Delta_g$) diatomic constants in Table 2. The constants were calculated by fitting the term values from Morrill *et al.*[41] using a non-linear least squares fit. The scans were fit assuming a Gaussian peak shape and the rotational distributions were obtained by fitting the peak heights and using line strength factor ratios calculated from the two-photon line strength equations from Bray and Hochstrasser,[50] neglecting the transition dipole factor. The ratios for S:R:Q:P:O

are 0.22:0.28:0:0.22:0.27 for J = 20. Variations from the calculated values are attributed to an inaccurate power correction. The Q branch is predicted to be weak, especially at high J and is not seen in the experimental results.

The overlapping states in the P and O branches were difficult to fit accurately, so the fits relied heavily on the isolated peaks of the R and S branches for the v = 0 scans. There is accidental overlap between the peaks in the R and S branches in the v = 1 scans, so the amount of peaks available to fit was less than expected. Since the line strength factor ratios for the S and R branch are very similar, the intensity for a given rotational state should be roughly the same for both branches. This fact was used to help assist in fitting the spectra where the braches overlapped. The rotational distribution for v = 0 at 282 nm peaks at lower J and converges at the bandhead. Towards the high J side of the S branch there are isolated peaks which were fit first before fitting the rest of the S branch and the isolated peaks of the R branch. The low J states overlap too much to confidently fit. For states J ≤ 6, accurate fits could not be determined. The best fit values are reported and error bars have not been provided for these states. The experimental and calculated rotational distributions have been area normalized. Suppression factors, S, were calculated using equation 3.1,

$$S = \frac{P(J_{even}) - P(J_{odd})}{P(J_{even})} \tag{3.1}$$

where the even J state population is defined as the average population of the two neighboring even states of the odd state. The suppression factor can range from 0

– 1 where 0 corresponds to no suppression and 1 corresponds to complete suppression of the odd state.

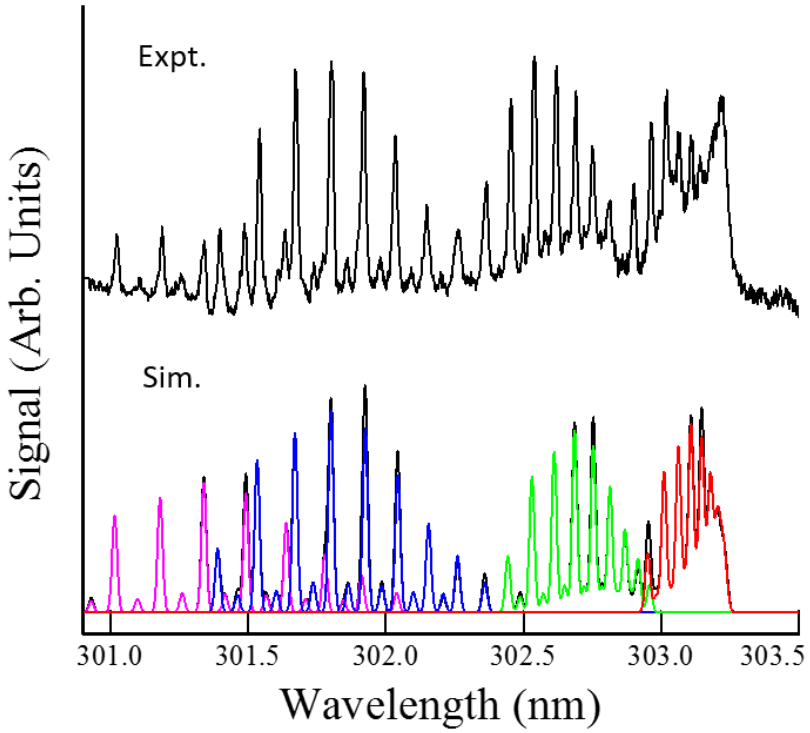

Figure 21: Experimental (top) and simulated (bottom) rotational spectrum for O_2 (a $^1\Delta_g$, v = 0) from the photolysis of O_3 at 248 nm. In the simulated spectrum, the branches are shown with difference colors: O (red), P (green), R (blue), S (pink). The sum of the branches is shown in black.

The rotational spectrum and simulation for O_2 (a $^1\Delta_g$, v = 0) at 248 nm is shown in Figure 21. The P, R, S, and O branches are observed. The O branch exhibits a bandhead while the majority of the peaks in the P branch are isolated. The R and S branches are at the low wavelength side of the scan and most of the peaks are isolated.

It is clear in the experimental spectrum that the intensity of every other state is much weaker than the neighboring states. After fitting the spectrum, it was found that the weaker states belong to the odd J states.

Rotational populations for the v = 0 spectrum were extracted and are shown in Figure 22 and are compared to the trajectory results reported by McBane *et al.*[22, 51] The distribution is peaked at high J (J = 30) and it is clear that the odd state populations are much lower than the even states. The population alternation is strongest at the peak of the distribution and weakens at the high and low J sides. Suppression factors ranged from 0.74 to 0.87. The trajectory results are peaked at J = 28 and are slightly broader than the experimental results. It was difficult to fit the low and high J states due to the states overlapping, so there may be a small population at the high and low sides of the experimental distribution that was unable to be fit. The calculations did not include the population alternation so the trajectory results should represent averages of the even and odd experimental distributions. This is approximately what occurs in Figure 22 and is similar for all the distributions.

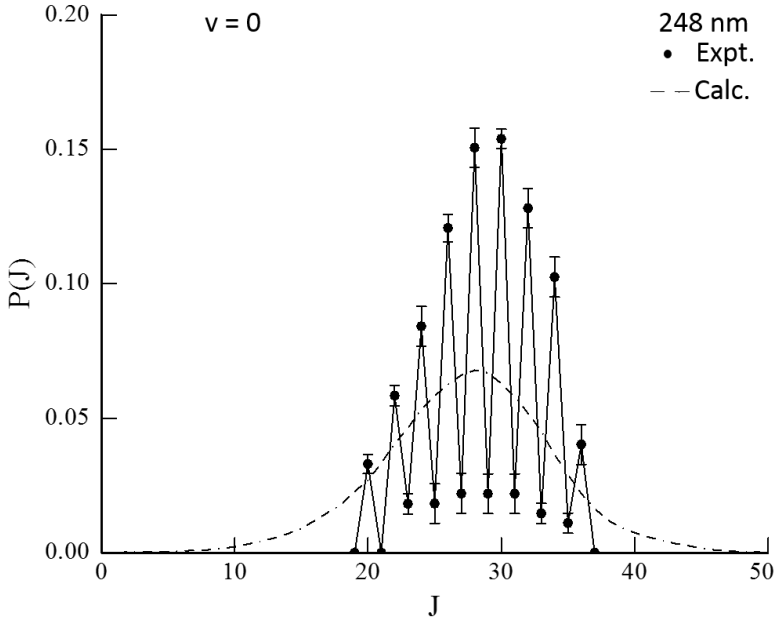

Figure 22: The rotational distribution for O_2 (a $^1\Delta_g$, v = 0) from the photolysis of O_3 at 248 nm (filled circles). The trajectory results reported by McBane *et al.* in Ref. 22 are shown with the dashed line.

Figure 23 shows the rotational spectrum for O_2 (a $^1\Delta_g$, v = 1) at 248 nm. The entire R and S branches are shown along with the high J side of the P branch. The peak marked with an asterisk is a reproducible, non-resonant peak and is not assigned to a specific rotational state. There is accidental overlap of peaks in the R and S branches, so there are fewer peaks than expected. The population alternation is still very strong for O_2 v=1. The peak of the rotational distribution (Figure 24) has shifted to lower J (J = 22) since the speed of the fragments has decreased. The distribution is broader which may be due to the fact that the overlapping states of the R and S branches made fitting the scan more difficult, particularly for the low rotational states. The experimental results

agree with the calculated results well. The trajectory results are peaked at J = 24 and are slightly narrower. The alternation is still very strong and suppression factors range from 0.70 – 0.84.

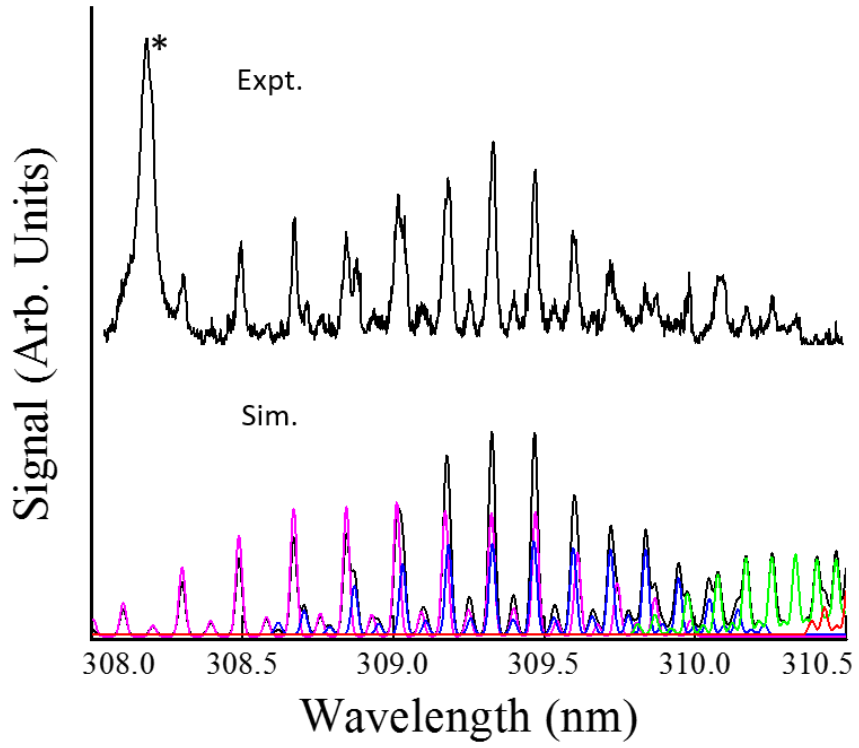

Figure 23: Experimental (top) and simulated (bottom) rotational spectrum for O_2 (a $^1\Delta_g$, v = 1) from the photolysis of O_3 at 248 nm. In the simulated spectrum, the branches are shown with difference colors: P (green), R (blue), S (pink). The sum of the branches is shown in black

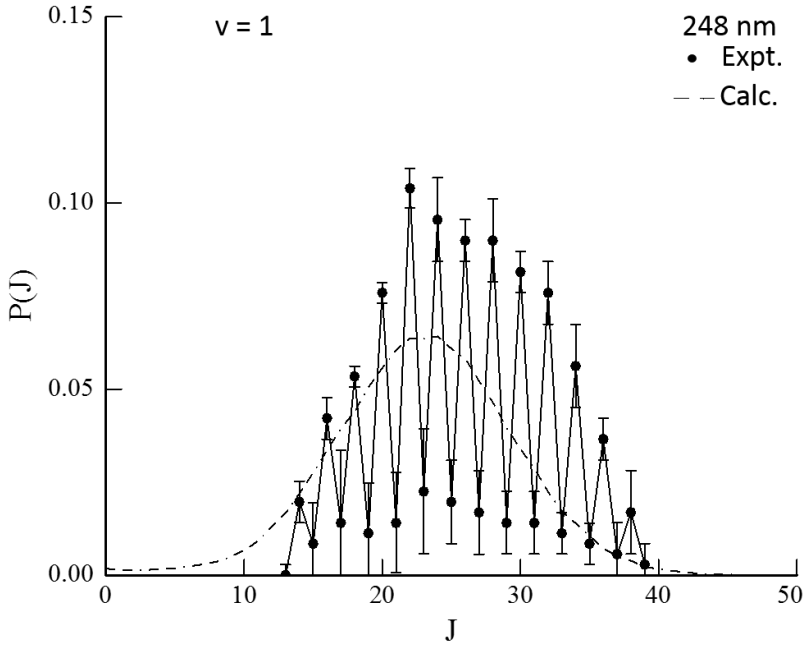

Figure 24: The rotational distribution for O_2 (a $^1\Delta_g$, v = 1) from the photolysis of O_3 at 248 nm (filled circles). The trajectory results reported by McBane *et al.* in Ref. 22 are shown with the dashed line.

The rotational spectrum for v = 0 following the 266 nm photolysis of ozone is shown in Figure 25. The P, R, O, and S branches are observed and the O and P branches have a bandhead. Since the speed of the fragments is lower at longer photolysis wavelengths, the rotational distribution has shifted to lower J and is starting to converge at the bandheads. Some of the peaks in the R and S branches overlap. The rotational spectrum was difficult to fit since so many states overlap. The rotational distribution is shown in Figure 26. The peak in the rotational distribution has shifted to J = 22. The population alternation is still present in the experimental results. The magnitude of the alternation has not changed much with suppression factors that

range from 0.74 to 0.96. The trajectory results are peaked at an odd J state, J = 21, since the population alternation is not present. The most populated even state is J = 22. The widths of the two distributions are very similar, however there is a small population in the low J states for the trajectory results which does not appear to present in the experimental data.

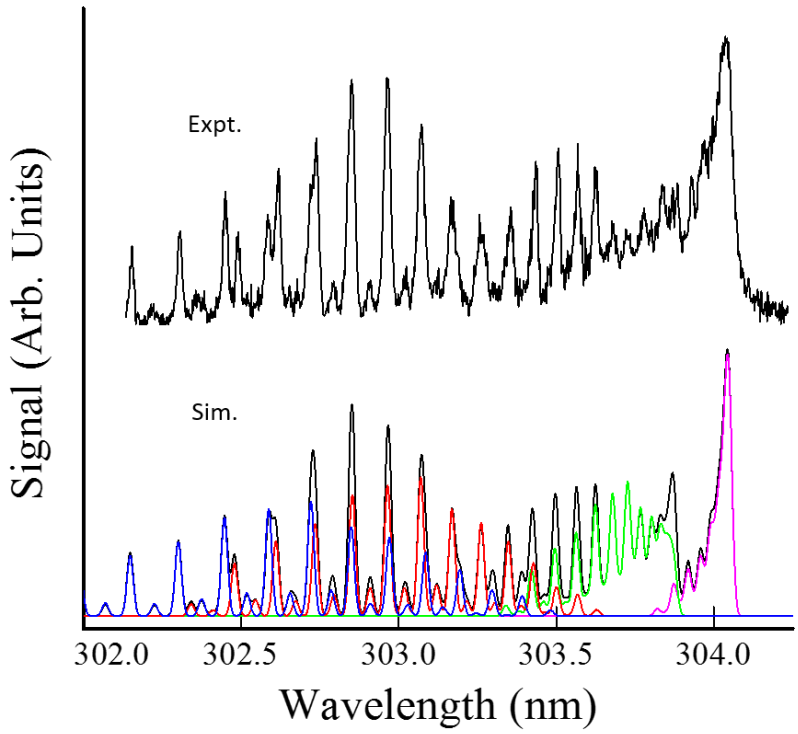

Figure 25: Experimental (top) and simulated (bottom) rotational spectrum for O_2 (a $^1\Delta_g$, v = 0) from the photolysis of O_3 at 266 nm. In the simulated spectrum, the branches are shown with difference colors: O (pink), P (green), R (red), S (blue). The sum of the branches is shown in black.

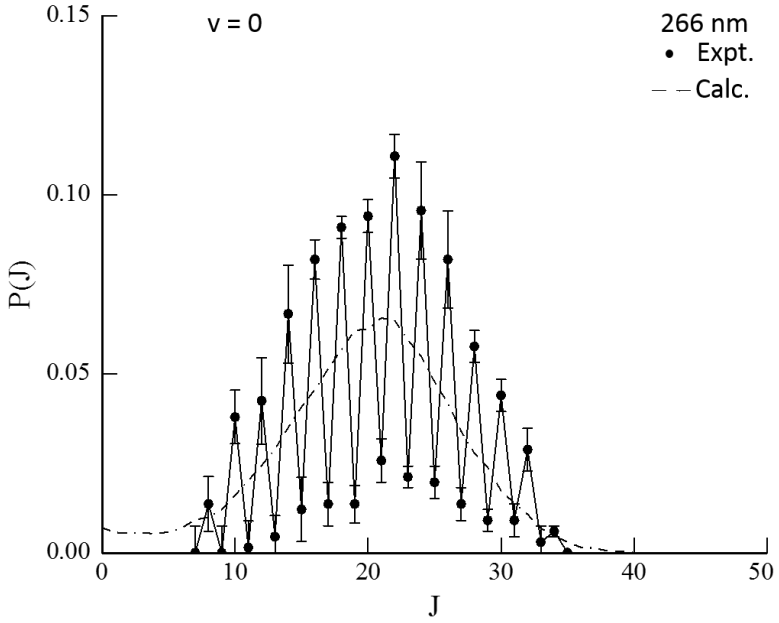

Figure 26: The rotational distribution for O_2 (a $^1\Delta_g$, v = 0) from the photolysis of O_3 at 266 nm (filled circles). The trajectory results reported by McBane *et al.* in Ref. 22 are shown with the dashed line.

The rotational spectrum for v = 1 at 266 nm (Figure 27) shows the R and S branches. Although a few of the peaks overlap, the majority are sufficiently isolated to be reliably fit. The population of the odd J states is still significantly lower than the neighboring even states. The population alternation is very clear in the rotational distribution shown in Figure 28, corresponding to suppression factors in the range of 0.69 to 0.89. The distribution is peaked at J = 18 which has shifted to lower J. For an impulsive model, it is expected that the peak of the distribution would shift to lower J due to lower available energy. However, the peak shifts to lower J for ozone photodissociation because the torque from the B state bending potential reduces the

fragment angular momentum. This effect is more significant for fragments with lower kinetic energy. The trajectory results peak at J = 17, but the most populated even state is J = 16. The population at low J is greater for v = 1. The population appears to start increasing again at low J. The low J states were difficult to fit since they were not well isolated. However, the increase in population did not appear to be present in the experimental results. It was assumed that the low J side of the distribution decreases monotonically, but the low J increase in population predicted by theory cannot be ruled out.

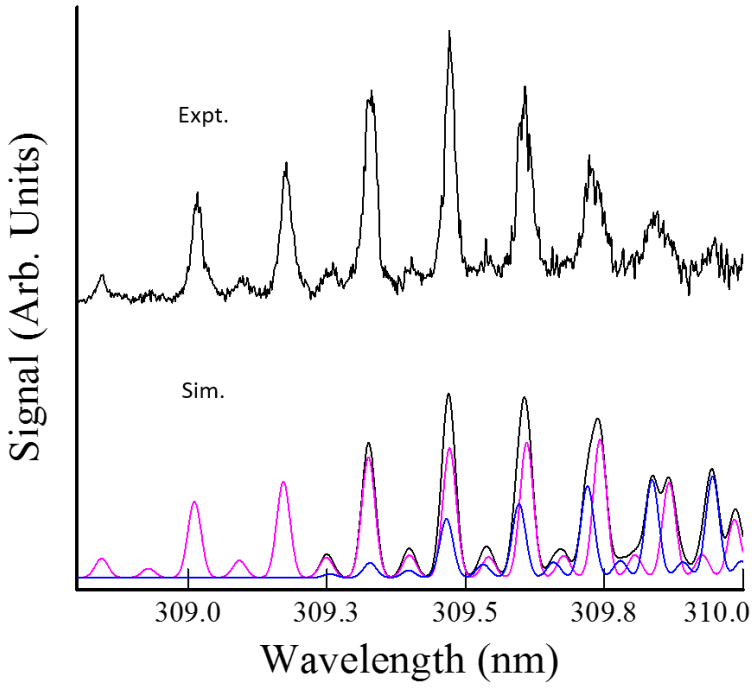

Figure 27: Experimental (top) and simulated (bottom) rotational spectrum for O_2 (a $^1\Delta_g$, v = 1) from the photolysis of O_3 at 266 nm. In the simulated spectrum, the branches are shown with difference colors: R (blue) and S (pink). The sum of the branches is shown in black

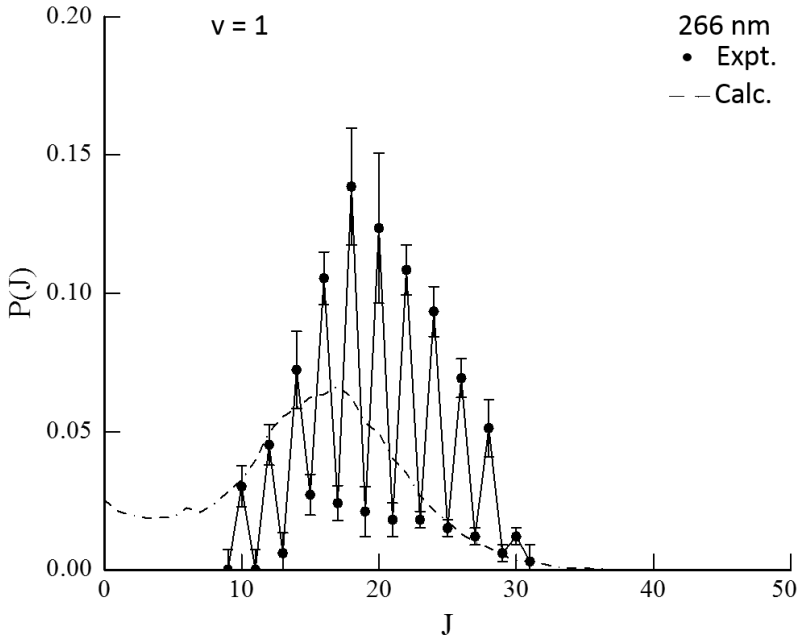

Figure 28: The rotational distribution for O_2 (a $^1\Delta_g$, v = 1) from the photolysis of O_3 at 266 nm (filled circles). The trajectory results reported by McBane *et al.* in Ref. 22 are shown with the dashed line.

The rotational spectrum for v = 0 from the 282 nm photolysis of ozone is shown in Figure 29. Since the fragment speed has decreased, the B state bending potential has a large effect and the peak of the rotational distribution has shifted to lower J. The peaks in the rotational spectrum have converged in the bandheads of the P and O branches which makes it difficult to fit. There are some isolated peaks in the S branch. Even though many states overlap, it is still clear that the population alternation is still present. The rotational distributions are shown in Figure 30. The low J states were difficult to accurately fit and it was assumed that the populations decreased on both sides of the distribution. For states J ≤ 6, the best fits are shown with open circles. No

error bars are reported for these states. The distribution is peaked at J = 10 and the suppression factors are still very strong ranging from 0.53 to 0.87. For the higher J states, the trajectory results agree well, but there is disagreement for the low J states. For v = 0 at 282 nm, the increase in population for low J states is very apparent for the calculated results. The increase is so sharp that the peak of the distribution is J = 0. It was difficult to fit the low J states, so the population increase may be present, but was not consistent with the expected results.

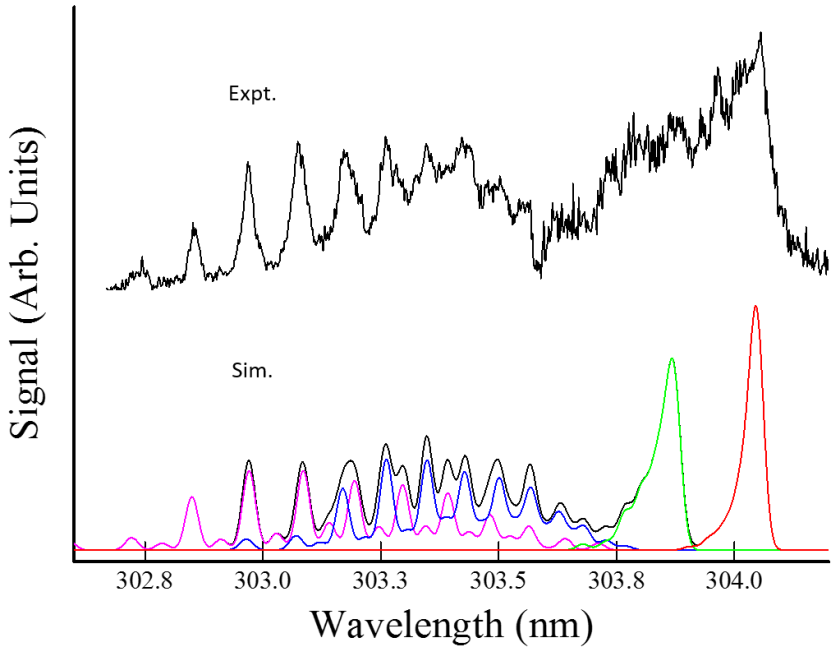

Figure 29: Experimental (top) and simulated (bottom) rotational spectrum for O_2 (a $^1\Delta_g$, v = 0) from the photolysis of O_3 at 282 nm. In the simulated spectrum, the branches are shown with difference colors: O (red), P (green), R (blue), S (pink). The sum of the branches is shown in black.

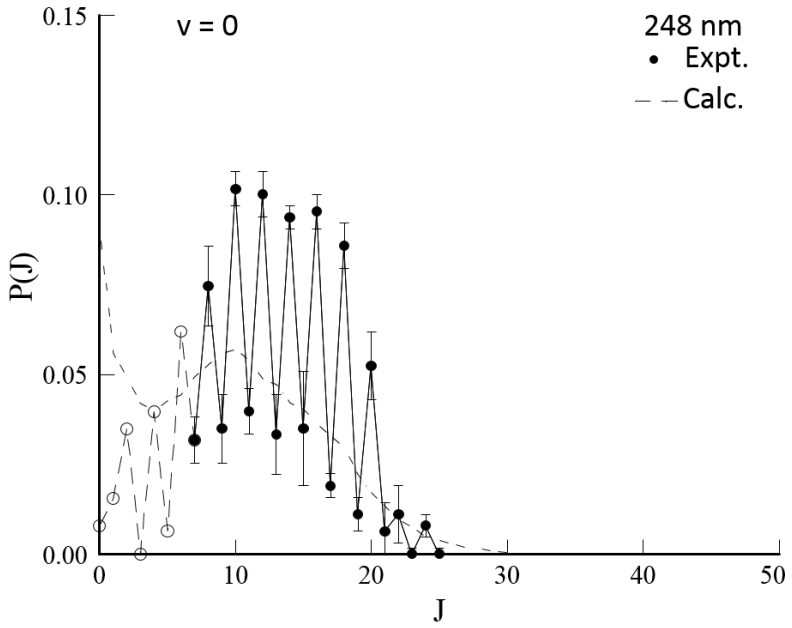

Figure 30: The rotational distribution for O_2 (a $^1\Delta_g$, v = 0) from the photolysis of O_3 at 282 nm (filled circles). The trajectory results (Ref. 51) are shown with a dashed line.

Rotational distributions have been measured by Valentini *et al.*[13, 52] using coherent anti-stokes raman spectroscopy (CARS) following ozone photolysis in the Hartley band. Theoretical studies[17, 20-23, 27] have also obtained O_2 (a $^1\Delta_g$) rotational distributions and compared the results to those of Valentini *et al.*[13] The rotational distributions are peaked at high J and shift to lower J as the photolysis wavelength and O_2 v state are increased. Valentini modeled the dissociation as vibrationally adiabatic and rotationally impulsive since the rotational distributions peaked at high J and the vibrational distributions peaked at v = 0.[53] However, Qu *et al.*[23] demonstrated that the agreement between the impulsive model and the rotational distribution was simply

fortuitous. The authors show that the strong torque on the B state limits the free rotation of the O_2 fragment and the ratio of rotational and available energies is less than that predicted from the impulsive model.

The rotational distributions reported in this dissertation are qualitatively consistent with the previous experimental results. The distributions are peaked at high J and shift to lower J as the effect from the B state potential becomes more significant and the width of the distributions are also similar. One feature of the rotational distributions that has caused considerable debate is the even/odd J state intensity alternation observed in the early experiments of Valentini *et al*.[13] The alternation shows an uneven distribution of even and odd J state populations where the even state populations are consistently greater than the odd state populations. Valentini *et al.*[13] observe an alternation that is greatest at short photolysis wavelengths and low O_2 (a $^1\Delta_g$) vibrational states. The alternation also appears to be J state dependent; it is strongest at the peak of the distribution and weakens at the edges for all distributions. The alternation for the present results only depends on J state and does not appear to significantly change with photolysis wavelength or O_2 (a $^1\Delta_g$) vibrational state. Valentini *et al.* attributed the intensity alternation to a selective depletion of the odd states due to the curve crossing from the B state to the R state leading to the O_2 ($^3\Sigma_g^-$) + O (^{3}P) channel. Only odd J states are allowed for the O_2 ground state due to symmetry constraints of the homonuclear diatomic.[13, 54] Because of this constraint, only odd J states can cross to the R state, resulting in a selective depletion of the odd states in the

O_2 (a $^1\Delta_g$) rotational distribution. CARS experiments were performed on the $^{16}O^{18}O$ products arising from the photodissociation of isotopically mixed ozone and the rotational distribution did not show a population alternation. For an isotopically heteronuclear O_2 fragment, there are no restrictions on the allowed J states in the ground state and all rotational states can couple to the R state, supporting the hypothesis of Valentini *et al*.

The B/R curve crossing is the only pathway to triplet products and if the crossing is solely responsible for the population alternation then the difference between the even and odd J state population should be an indirect measure of the triplet quantum yield. Valentini *et al.* calculated the triple yields using the following equation 3.2,

$$\frac{\sum_{Jeven} P(J_{even}) - \sum_{J_{odd}} P(J_{odd})}{2 \sum_{Jeven} P(J_{even})} \tag{3.2}$$

where the populations for the even and odd states were summed over all v states and weighted by the vibrational branching ratios. If the B/R curve crossing was entirely responsible for the alternation, it would be expected that the quantum yield of the triplet channel would change as the strength of the alternation changed. The strength of the alternation clearly decreases with increasing photolysis wavelength for the CARS results. This should correspond to an increase the quantum yield of the singlet channel and a decrease in the quantum yield for the triplet channel, assuming there are only two dissociation channels. However, the triplet quantum yields reported by Valentini *et al.*[13] were independent of wavelength over the range where the intensity of the

alternation changed. The quantum yield is also independent of parent internal energy. Sparks *et al.*[8] studied jet-cooled ozone photodissociation using photofragment translational spectroscopy (PTS) and determined the quantum yield for the triple channel was ~0.1. This agrees with the quantum yield obtained from the 300 K CARS experiment. Using the same method as Valentini *et al.*, the triplet quantum yield was calculated for the three photolysis wavelengths studied in this dissertation. Since the alternation is stronger for the jet-cooled ozone, the calculated triplet quantum yield should be significantly larger than the 300 K results based on equation 3.2 if the B/R crossing is the only explanation for the alternation. Although rotational distributions were not collected for every O_2 vibrational state, v = 0 and 1 accounted for ~80% of the population for 248 and 266 nm. The rotational and vibrational distributions were normalized before determining the quantum yield. The calculated quantum yield for the triplet channel ranged from 0.27 – 0.44 which is much greater than what has been observed previously. A summary of the calculated and measured[8, 13, 14, 55] triplet channel quantum yields are shown in Table 3. Since not all the vibrational states were measured, a lower and upper limit to the quantum yield was determined based on two limiting assumptions. The lower limit was calculated assuming the distributions for v > 1 had no suppression and the upper limit was determined assuming the distributions had total suppression. The triplet quantum channel was also calculated assuming the distributions for v > 1 had the same suppression as v = 0 and 1. The quantum yield study indicates that there is another explanation for the observed alternation in the

current molecular beam experiments. If the curve crossing was the only explanation for the alternation, it would be expected that the quantum yield of the triplet channel would increase with decreasing parent internal energy since the alternation becomes stronger, contrary to the observations. The quantum yield is also the same for jet-cooled and 300 K ozone.

Table 3: Calculated and measured quantum yields for the triplet channel.

Wavelength	Lower Limit	v = 0, 1 Suppression	Upper Limit	Indirect[a]	Direct
248 nm	0.35	0.42	0.44	-	0.10-0.15[b]
266 nm	0.36	0.41	0.43	0.15	0.12,[c] 0.10[d]
280 nm	-	-	-	0.08	-
282 nm	0.27	0.34	0.40	-	-

[a] Value from Ref. 13
[b] Value from Ref. 14
[c] Value from Ref. 55
[d] Value from Ref. 8

If the B/R crossing is modeled using the 1-D Landau-Zener crossing theory, the velocity will dictate the B/R crossing probability, shown in equation 3.3,

$$P_{cross} = e^{\left(\frac{-2\pi V_{12}^2}{\hbar v|\Delta F|}\right)} \quad (3.3)$$

V_{12} is the potential coupling of the B and R states, ΔF is the difference in slopes at the crossing point, and v is the radial velocity. The smaller the velocity, the higher the

crossing probability to the R state. This would increase the strength of the intensity alternation and increase the triplet quantum yield. This is precisely the opposite trend observed in the CARS results. The alternation is strongest, i.e. the crossing probability would be highest, for v = 0 at 240 nm where the velocity is greatest. As v increases, the velocity decreases and the alternation weakens which indicates the crossing probability is lower for lower fragment velocities. It is important to keep in mind that the crossing is really a seam and not a point, therefore a 1-D Landau-Zener model treatment should only be considered qualitatively.

Additional evidence also suggests that the trend with vibrational state observed by Valentini and co-workers is the opposite of what is expected. Not only does velocity dictate which molecules will cross to the R state, but the B/R crossing probability is higher for larger r_2, the bond length of the resulting O_2 fragment at the seam.[22] The equilibrium bond length for O_2 (a $^1\Delta_g$) is 1.21 Å, so molecules with large r_2 produce O_2 fragments in higher v states, consistent with a simple Franck-Condon model, since the bond is stretched more during the dissociation. Therefore, the probability of crossing to the R state increases with increasing v state. Picconi and Grebenshchikov[49] performed quantum mechanical calculations that included the symmetry restrictions at the B/R crossing seam. No alternation was present in their results. They also state that the crossing probability should be the smallest for v = 0 and the alternation should get more pronounced with increasing O_2 (a $^1\Delta_g$) v state. The crossing seam is around 1.74 Å which is near the bottom of the B state well. There could be additional torque that

alters the rotational distribution after the seam which could weaken the alternation. When r_2 is around 1.21 – 1.53 Å, which produces lower O_2 v states, perhaps the molecules are not affected by the B state bending potential and the rotational states and the alternation are not affected after the seam. However, at larger r_2 (1.48 – 1.74 Å), after the molecules cross the seam, the bending potential could have a larger effect and the rotational distribution might be altered. Fragments that would have produced an even J state could continue to increase in angular momentum, producing odd J states due to the bending potential after the seam. Such an effect would weaken the alternation and may contribute to the trend of weakening alternation with increasing v state. It is unclear how much of an effect the B/R crossing has on the alternation, but these observations do prove that the origin of the intensity alternation is more complex than a simple curve crossing mechanism involving the B and R states.

Our results show an intensity alternation that is greatest at the peak of the distribution, but does not appear to depend greatly on wavelength or O_2 (a $^1\Delta_g$) vibrational state. Another notable difference between the experimental results is the strength of the alternation. The present results show an alternation that is much stronger than that observed in the CARS experiments. The CARS experiment obtained a maximum suppression factor of 0.63 for v = 0 at 240 nm while the present results show a maximum suppression factor of 0.96. Determining the reason for this difference may help elucidate the origin of the alternation. The CARS experiment was performed for a 300 K sample while the molecular beam temperature was determined to be < 60 K. This

difference has led to the investigation of the effect of parent internal energy on the population alternation. Additional important evidence also suggests that parent internal energy has an effect on the intensity alternation. The dependence on J and v state and photolysis wavelength can be linked to parent internal energy effects. For the dependence of the alternation on v, J, and wavelength, parent molecules with more internal energy are preferentially photolyzed. The low and high O_2 J states come from the low and high sides of the O_3 rotational distribution. For a 300 K sample, the distribution is much broader compared to 60 K, so there are more available states to produce the J states at the tails of the O_2 distribution. The absorption cross section on the low energy side of the Hartley band increases with increasing temperature, therefore, wavelengths in this range are more sensitive to warmer parent molecules. Lastly, higher vibrational states of the O_2 fragment will more likely come from hot bands. All three of these trends would weaken the alternation and were observed in the CARS results. The only trend observed for the jet-cooled sample is the trend with O_2 J state.

The molecular beam temperature was calibrated using NO rotational spectroscopy. To explore the effects of parent internal energy, excitation to v' = 2 was used since difference in the alternation was of interest and not rotational populations. Due to the perturbation, the intensity alternation is not as strong in the (2, 0) band as the (4, 0) band. This change in the even/odd J state ratio allowed minor changes in the alternation to be detectable when the temperature of the beam was increased.

Temperatures in the range of 60 ± 10 to 200 ± 20 K were obtained. Scans of the (2, 0) band were obtained for the different beam temperatures and scans for the 60 and 200 K beams are shown in Figure 31. It was found that increasing the parent internal energy increased the odd J state population, diminishing the intensity alternation. At 60 K, the suppression factor was 0.58 and at 200 K the alternation disappeared for the (2, 0) band. The alternation should not disappear for the (4, 0) band at 200 K since the alternation is much stronger for excitation to v' = 4. This is exactly what was found. The alternation appeared to weaken for the (4, 0) band when the temperature was increased, but the changes were much smaller than the (2, 0) band. This partially explains the different strengths of the alternation that were observed in the CARS and molecular beam experiments. Since ozone molecules had more internal energy in the CARS experiment, the odd states were more populated and the alternation was weaker. This result cannot rule out curve crossing as an explanation for the alternation, but it does indicate that parent internal energy is an important factor to consider when determining the origin of the intensity alternation.

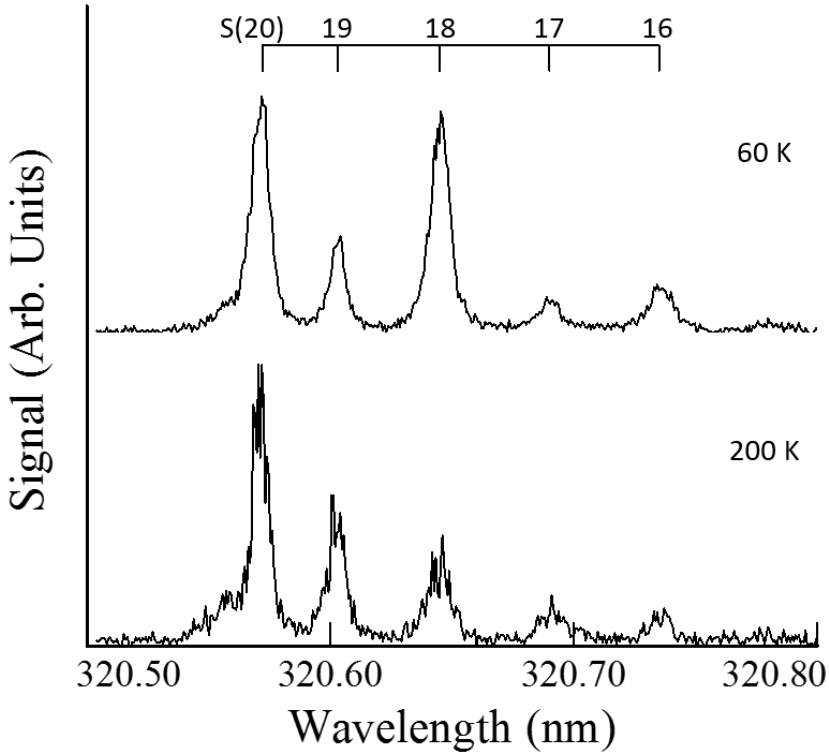

Figure 31: REMPI spectra of O_2 (a $^1\Delta_g$, v = 0) following the 266 nm photolysis of ozone via the O_2 (d $^1\Pi_g$, v = 2) ←← O_2 (a $^1\Delta_g$, v = 0) transition for a 60 and 200 K beam temperatures.

Baloïtcha and Balint-Kurti[17] have given an alternative explanation for the observed alternation stating that careful consideration of the initial wavefunction of the ozone molecule and the dissociative wavefunction of the molecule in its excited state should be taken into account. Assuming a parent molecule with zero total angular momentum, due to the allowed symmetries of the wavefunctions, only even J states should be allowed in the O_2 (a $^1\Delta_g$) rotational distribution. Relaxation of the symmetry constraints for ozone molecules with nonzero total angular momentum would allow the odd J state population to increase. This explanation is consistent with the

observations, however, the quantum mechanical calculations performed by Picconi and Grebenshchikov[49] did not show any alternation. Based on their calculations, neither the symmetry constraints nor the curve crossing cause a population alternation. The fact that theory has been unable to reproduce the alternation proves that the mechanism responsible for the population alternation is more complex than the proposed explanations.

The curve crossing occurs at short r_1, near the bottom of the B state well. At this point, the resulting O_2 (a $^1\Delta_g$) fragment does not have a well-defined rotational state. The fragment angular momentum is still evolving and any alternation that may be present due to a preference for odd states at the curve crossing could be lost. The curve crossing may not cause any population alternation and the fact that the quantum yield of the triplet channel was calculated using the difference in population of the even and odd states could be fortuitous. The explanation of symmetry restrictions accounts for the observations and takes into account the importance of parent internal energy, but if it was causing the alternation, it would be expected that a population alternation would be present in the calculations of Picconi and Grebenshchikov.[49] The origin of the population alternation is still unknown, but the molecular beam experiments have provided a new set of observations that are very important. Based on the new observations, it is clear that a simple curve crossing does not account for the majority of the alternation. It is still to be determined if the crossing seam is responsible for any alternation, but it is now known that parent internal energy plays

an important role in the population alternation. The new experimental results provide a detailed set of observations which represent a challenge and rigorous test of future theoretical studies on ozone photodissociation.

CHAPTER IV

O_2 VECTOR CORRELATIONS

The properties measured in photofragment spectroscopy can be classified as either scalar or vector quantities. Scalar properties describe the energy partitioning into the available degrees of freedom while vector properties describe the direction and magnitude of a particular motion. The angular distribution observed in an ion image is due to the dynamics of the photodissociation and can be described by three vectors: the transition dipole moment of the parent, μ; the recoil velocity of the fragment, v; and the rotational angular momentum of the fragment, J. Correlations between these vectors provide insight into the dynamical processes.

The bipolar moment parameters, $\beta_Q^K(k_1 k_2)$, for describing the semi-classical dynamics of direct photodissociation described by Dixon,[56] have been adopted to interpret the vector correlations. The bipolar moments are expansion coefficients in a bipolar harmonic expansion of the spatial probability distribution of v and J in the frame on μ. For a one-photon dissociation and two-photon probe scheme, there are nine bipolar moments, but only $\beta_0^2(20)$, $\beta_0^2(02)$, and $\beta_0^0(22)$ can be conveniently described as the expectation value of the 2nd Legendre polynomial, $\langle \mathrm{P}_2(\cos\theta) \rangle$, where θ is the angle between the two relevant vectors. The limiting values of the bipolar moments are -0.5 – 1 when the vectors are perpendicular or parallel respectively.

The probability of a molecule absorbing a photon is proportional to $|E \cdot \mu|^2$, where E is the electric field of the laser. Therefore molecules with μ parallel to the electric field of the laser, E, will preferentially absorb a photon and dissociate. This aligns the parent molecules in the lab frame and the angular distribution for a one-photon process can be described by equation 4.1,

$$I(\theta) = \frac{1}{4\pi}[1 + \beta P_2(cos\theta)] \quad (4.1)$$

where $P_2(cos\theta)$ is the 2nd Legendre polynomial, θ is the angle between the recoil velocity and the electric field of the laser, and β describes the degree of anisotropy ($-1 \leq \beta \leq 2$). For a diatomic molecule, μ will either be parallel or perpendicular to the bond. If the molecule dissociates quickly relative to the rotational period of the parent, the fragment recoil velocity will also be parallel or perpendicular to μ. A limiting value of β = -1 corresponds to a purely perpendicular transition (μ perpendicular to the breaking bond) while β = 2 corresponds to a purely parallel transition (μ parallel to the breaking bond). Non-limiting values of β can due to a long dissociative lifetime or a mixed transition. Additionally, for a polyatomic molecule, the recoil velocity may have an angle, α, to μ which will also produce non-limiting values of β.

$\beta_0^2(20)$, the μ-v correlation, describes the direction the fragments are ejected with respect to the transition dipole moment of the parent. Zare and Herschbach[57] first considered that the correlation of μ with v was important for photodissociation in 1963 and in 1967, Solomon[58] was the first to observe an anisotropic distribution of recoil

velocities. Bromine or iodine were photolyzed with a linearly polarized laser in a hemispheric bulb coated with a thin file of tellurium. The atoms were ejected perpendicular to the electric field of the laser and they etched the angular distribution into the tellurium coating. The anisotropy parameter, β, is related to the μ-v correlation by $\beta = 2\beta_0^2(20)$. The μ-v correlation is often referred to as the spatial anisotropy and can provide information about the symmetry of the excited state and dissociative lifetime.

Similar to the fragment velocity, the rotational angular momentum of the fragment can be aligned in the lab frame and is strongest for a fast dissociation. Referred to as rotational alignment, $\beta_0^2(02)$ or the μ-J correlation describes the relative spatial orientation of the parent molecule and the fragment rotational plane. Since v and J are each correlated to μ, it is no surprise that they can be correlated to each other. Both v and J are properties of the photofragment and therefore do not depend on the parent molecule. $\beta_0^0(22)$ (the v-J correlation) is a result of torques and forces as the molecule dissociates and is not affected by long dissociative lifetimes and parent rotation prior to dissociation. The terms cartwheeling and helicoptering are used for the limiting cases when v⊥J or v∥J respectively. For the dissociation of a non-rotating triatomic molecule, v must be perpendicular to J, so the limiting value of -0.5 is obtained. This is true because the orbital angular momentum is perpendicular to the transition dipole moment. Angular momentum must be conserved, so the fragment angular momentum must be opposite in direction to the parent orbital angular

momentum. For ozone, μ is in the plane of the molecule so the recoil velocity is also in the plane. The impulse of the dissociation is along the breaking O – O bond and provides a torque on the molecular fragment. There is no motion that provides an out-of-plane torque, so the O_2 fragment rotates in the plane of the parent molecule and J is perpendicular to v. For a rotating parent molecule ($J \neq 0$), the v-J correlation will no longer be the limiting value of -0.5.

The transition dipole moment of ozone lies parallel to the line connecting the two end atoms as shown in Figure 32. Suits *et al.*[10] was one of the first to study the vector correlations from the photodissociation of ozone. Ion images of the O_2 (a $^1\Delta_g$) fragment were obtained and the images were simulated using a Monte Carlo forward convolution. To simulate the images, the dissociation was modeled using the impulsive model and the calculated value for the spatial anisotropy ($\beta = 1.18$) was used. It was also assumed there was no triple vector correlation (μ-v-J). The only adjustable parameter was the O_2 rotational state, J. The impulsive picture predicts the v-J limiting value of -0.5 ($v \perp J$) will be closely approached. This is expected for the dissociation of a jet-cooled triatomic molecule. Vector correlations were not directly determined in this study, but it was shown that ion imaging experiments can be exploited in vector correlation studies.

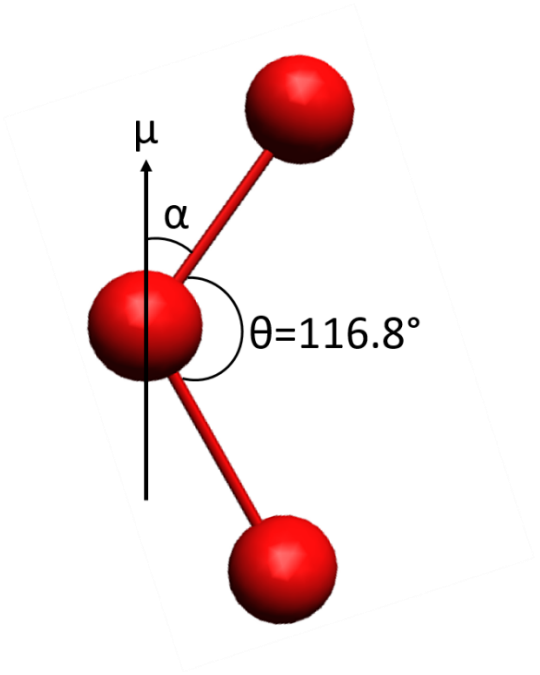

Figure 32: The transition dipole moment, μ, for ozone lies parallel to the line connecting the two end atoms. θ denotes the bond angle and α is the angle that will determine the anisotropy.

The anisotropy parameter, β, is directly related to the bond angle of ozone at the time of dissociation and has been measured numerous times.[2, 3, 5, 12, 59] For ozone dissociation, β ranges from ~1.2 at 235 nm to ~1.8 at 298 nm as determined by ion imaging experiments.[2] The increase of β with increasing wavelength indicates the bond opens during dissociation. Initially, the bond for every trajectory decreases close to the equilibrium bond angle of the B state, 107°. Late in the trajectory, the B state bending potential causes a torque on the molecule which then opens the bond. As the photolysis wavelength increases, the bending potential on the B state has a more

significant effect because the fragments have lower kinetic energy. The bond opens more and the fragments are ejected more parallel to the transition dipole moment.

Another set of experiments that has studied vector correlations in the O_2 fragment has shown an interesting feature.[3, 4] The anisotropy parameter is similar for every even/odd J state pair studied, but there are differences in the v-J and μ-J correlation. The values for the odd state are consistently more depolarized compared to the even state. The magnitude of the difference between the vector correlations is dependent on the speed of the fragment. The difference between the vector correlations increases with decreasing fragment speed. The odd J states are associated with the O_2 (a $^1\Delta_g^-$) Λ doublet while the even states are associated with the O_2 (a $^1\Delta_g^+$) Λ doublet. A possible explanation for the difference in the v-J and μ-J correlations between the even and odd states is that the Λ doublets may arise from two different pathways and parent rotational motion may affects the pathways differently. Any out-of-plane motion in the ozone molecule will depolarize the v-J correlation. Similar to OH from the photolysis of water,[60] the $^1\Delta_g^-$ Λ doublet may preferentially be formed from parent molecules with a larger component of their rotational angular momentum about axes within the molecular plane. This could depolarize the v-J of the odd state more compared to the even state.

Vector correlations from the photodissociation of ozone are of interest for two reasons. First, they were used as a test case for the extension of the one-photon speed-dependent vector correlation equations to two-photon processes. Grubb *et al.*[61]

presented analytical expressions relating bipolar moments to the measured anisotropy parameters of sliced ion images to extract speed-dependent vector correlations. These equations are only suitable for 1 + 1 REMPI, however, it is often required that a 2 + 1 REMPI scheme is used. Recently, the analytical expressions have been extended to allow the determination of speed-dependent vector correlations for a two-photon process. It was necessary to test the equations against a well-studied system. The vector correlations from ozone photolysis have been previously measured making ozone a good system to test the equations. More importantly, the vector correlations can provide valuable insight to help identify the origin of the even/odd J state population alternation better. Vector correlations can reveal which type of parent rotational motion is contributing to the production of the even and odd states. Ozone rotation about different axes will affect the vector correlations differently. Rotation in the molecular plane (J_c axis) will depolarize the μ-v correlation, but will not affect the v-J correlation. Conversely, out-of-plane rotation (J_a axis) will not affect the μ-v correlation, but will depolarize the v-J correlation. If the even and odd J states arise from different pathways, the out-of-plane may be more important in the formation of the odd states and therefore might depolarize the v-J correlation of the odd states while the v-J correlation of the even states may not be affected as much. This could lead to the observed v-J correlation alternation.

To determine the vector correlations, images from three laser polarization geometries for a given rotational state are needed. The polarization for the 266 and

282 nm lasers was controlled using a double Fresnel rhomb and the polarization of the 248 nm laser was controlled with a pile-of-plates polarizer. To ensure the lasers were nearly 100% polarized, a Glan-Taylor polarizer was used to remove any of the unwanted polarization. There is a total of four laser geometries because the laser can be polarized vertical (parallel to the imaging plane) or horizontal (perpendicular to the imaging plane). The three images needed are the VV, VH, and HV were the first letter refers to the polarization of the dissociation laser and the second refers to the polarization of the probe laser. If both lasers are perfectly polarized, the HH image will have an isotropic angular distribution. The image does not provide any information and is not needed to calculate vector correlations. It does, however, provide a check of the laser polarizations. If the lasers are not perfectly polarized, the image will not be isotropic and the vector correlations determined from the other images will not be accurate. After dissociation and ionization of the O_2 (a $^1\Delta_g$) fragments, the ions are accelerated down the TOF tube where they hit the position sensitive detector (MCP/phosphor screen). A CCD camera records the image and sends it to the computer where an image accumulates. After the signal to noise is sufficient, the polarization of the lasers can be changed and another image can be collected.

The O_2 images were not perfectly circular and had to be corrected before analysis. The deviation from a circle is most likely due to space-charge effects in the ion cloud. The images were imported into ImageJ[62] and were slightly stretched along one axis. The image was then cropped to 768 x 768 pixels. A set of four crushed ion images

for O_2 (a $^1\Delta_g$, v = 0, J = P(32)) are shown in Figure 33. Both the VV and HV images show four-fold symmetry where the majority of the signal is located in each quadrant of the image. To acquire an image with four-fold symmetry, a minimum of two photons is required. The VH image shows a typical $P_2(\cos\theta)$ angular distribution while the HH is isotropic. As stated previously, the HH laser polarization geometry must provide an isotropic distribution. Figure 34 shows a set of four images of O_2 (a $^1\Delta_g$, v = 0, J = S(19)) from the 266 nm photolysis of ozone. Since a different rotational branch is probed, the angular distributions are difference, but the analysis still produces accurate vector correlations.

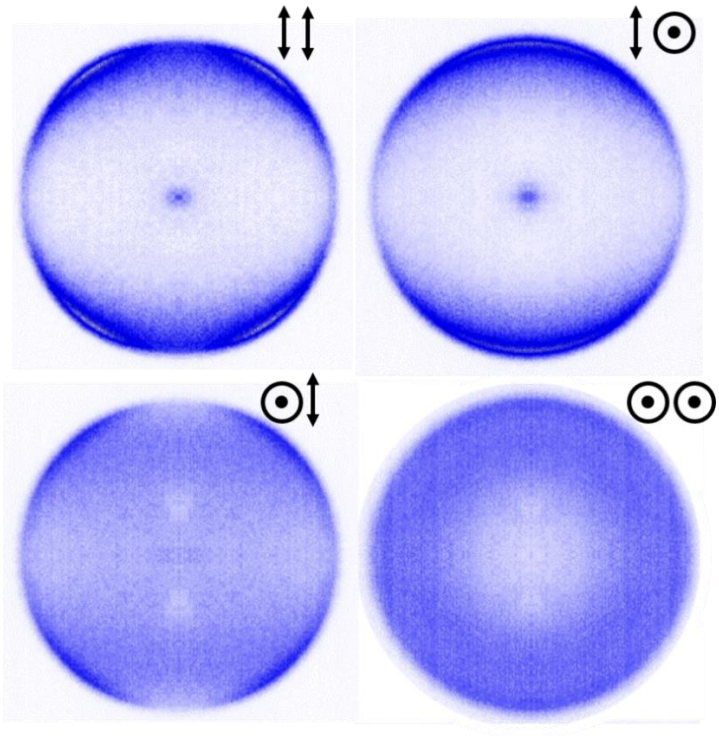

Figure 33: A set of images for O_2 (a $^1\Delta_g$, v = 0, J = P(32)) following the 248 nm photolysis of ozone. The four images are from the different laser polarization geometries. The first and second symbols are for the dissociation and probe laser respectively.

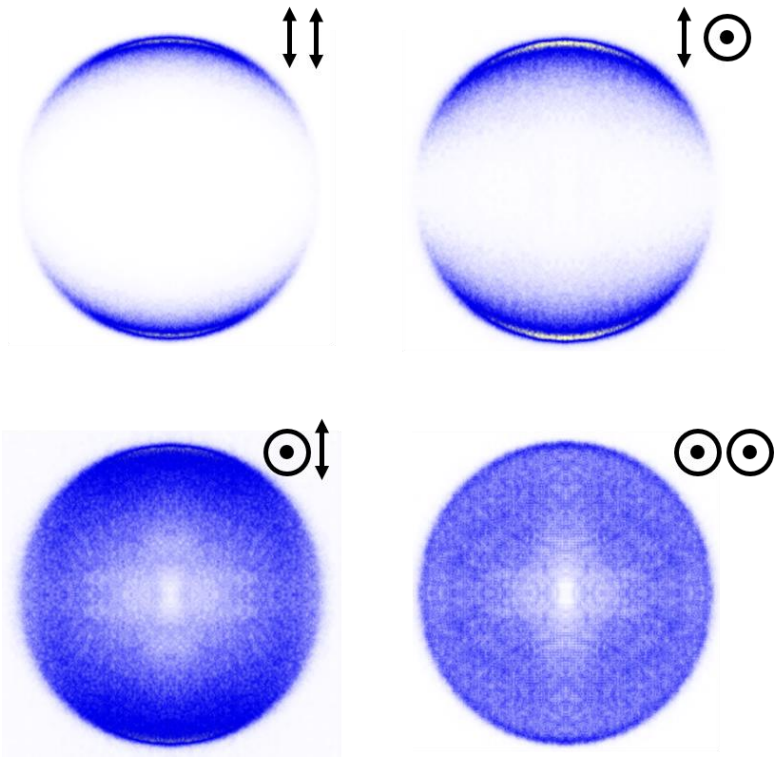

Figure 34: A set of images for O_2 (a $^1\Delta_g$, v = 0, J = S(19)) following the 266 nm photolysis of ozone. The four images are from the different laser polarization geometries. The first and second symbols are for the dissociation and probe laser respectively.

Angular distributions were extracted from each image by integrating the intensity over a narrow radial range (~7 – 9 pixels) around the outer edge of each crushed image. Grubb *et al.*[61] has determined that when the ion image consists of a single speed component, the signal at the maximum radius is equivalent to the angular distribution that would be obtained from a sliced image. Therefore, a narrow radial range from a crushed image can be analyzed like a sliced image. Once the angular distribution was obtained, it was fit with a forward convolution method using the

equations in the appendix. It is expected that the $\beta_0^2(24)$ parameter is nearly zero, so it was set to zero to obtain the angular distribution fits. The adjustable parameters were the ratios of the five limiting cases for the three vectors: μ, v, and J (Figure 35). The ratio of the cases was adjusted until the best fit was found. Case B, where μ∥v⊥J, had the most significant contribution.

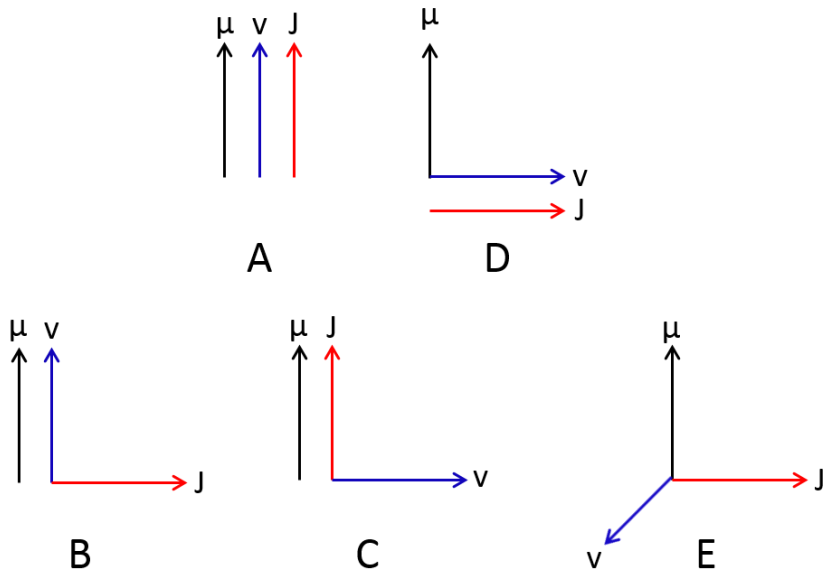

Figure 35: The five limiting cases for the transition dipole moment (μ), the velocity of the fragment (v), and the rotational angular momentum of the fragment (J).

The best fit was determined by minimizing the chi-square values for the three images. An example of the angular distribution fits for a set of images is shown in Figure 36. The S branch does not show four-fold symmetry. Instead the signal in the HV and VV images

is isolated to the top and bottom of the image in a $P_4(\cos\theta)$ distribution. The forward convolution method provided very good fits for most of the data. For the signal from the P branch where the HV and VV images show four-fold symmetry, the fits were not as good for the HV image.

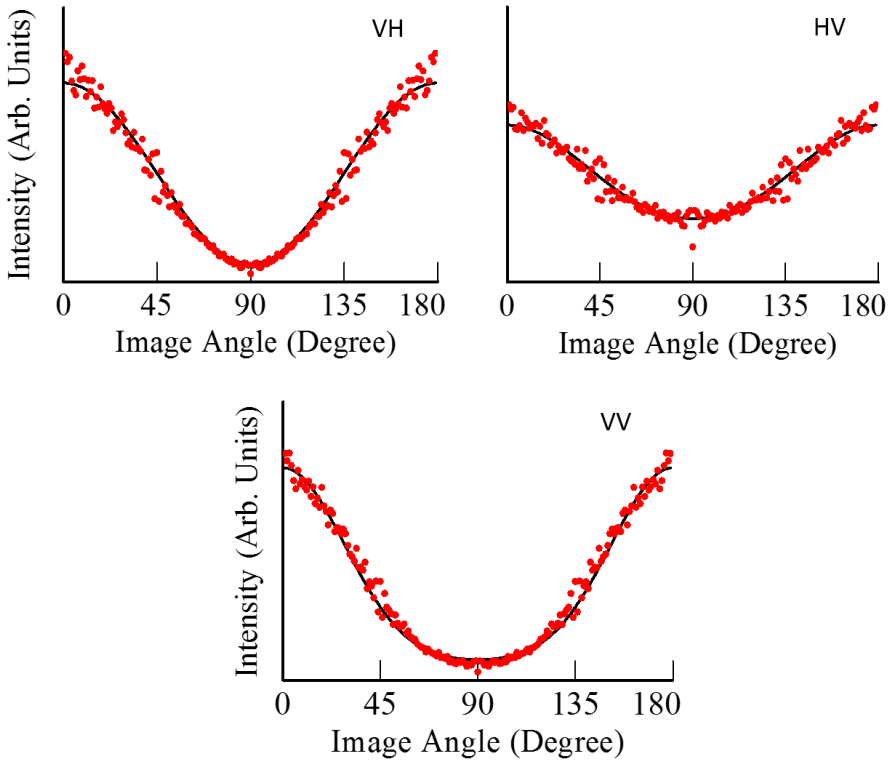

Figure 36: Forward convolution fits to the angular distributions for S (19) from the 266 nm photolysis of 60 K ozone. The fits are shown with a solid line and the data is shown with red circles.

The vector correlation results for the photolysis of ozone at 248, 266, and 282 nm are shown in Table 4, Table 5, and Table 6 respectively. The spatial anisotropy (μ-v)

is very similar for the even and odd states. The only even/odd pair of states that are not the same are v = 1 at 248 nm. The odd state is more depolarized relative to the even state. Although the fit to the angular distributions was acceptable, the signal for the odd state was low. When the temperature was increased, the μ-v correlation of the even and odd states was depolarized equally. When the internal energy of the parent is increased, it is expected that the vector correlations will be slightly depolarized due to parent rotation and translation which is observed. This is consistent with previous observations.[3, 4] Most of the values agree well with previous studies, but the μ-v correlation is a little lower for the 248 nm results (~0.46 vs. ~0.6). The beam that day may have been slightly warmer than usual which would depolarize the spatial anisotropy. Also, the angular distribution fits for the HV image for the v = 0 states at 248 nm did not fit as well as the other states. The spatial anisotropy for v = 0 at 266 nm increased to 0.71 while it decreases to 0.55 at 282 nm. The spatial anisotropy has been found to increase with decreasing wavelength until ~300 nm where it decreases sharply. While the value at 266 nm follows the trend, the 282 nm value is slightly lower than expected, but is still reasonable compared to previous results.

The alignment, μ-J, has a near limiting value (-0.5) for all of the states probed. When the beam temperature was increased, the μ-J was depolarized equally for both the even and odd states. Horrocks *et al.*[4] observed an alternation of the alignment parameter for consecutive even and odd J states, but no significant alternation is present in the current results.

Table 4: Vector correlations for O_2 (a $^1\Delta_g$) following the 248 nm photolysis of O_3 for a 60 K and 200 K beam.

State	Temperature	$\beta_0^2(20)$	$\beta_0^0(22)$	$\beta_0^2(02)$
v = 0, P(32)	60 K	0.47 ±0.05	-0.38 ±0.02	-0.50 ±0.05
	200 K	0.42 ±0.07	-0.36 ±0.02	-0.50 ±0.05
v = 0, P(33)	60 K	0.46 ±0.04	-0.36 ±0.02	-0.50 ±0.05
	200 K	0.46 ±0.03	-0.37 ±0.02	-0.50 ±0.05
v = 1, P(31)	60 K	0.23 ±0.03	-0.28 ±0.07	-0.45 ±0.09
	200 K	-	-	-
v = 1, P(32)	60 K	0.52 ±0.06	-0.42 ±0.07	-0.48 ±0.09
	200 K	-	-	-

Table 5: Vector correlations for O_2 (a $^1\Delta_g$, v = 0) following the 266 nm photolysis of O_3 for a 60 K and 200 K beam.

State	Temperature	$\beta_0^2(20)$	$\beta_0^0(22)$	$\beta_0^2(02)$
S(19)	60 K	0.71 ±0.02	-0.40 ±0.05	-0.48 ±0.02
	200 K	0.47 ±0.03	-0.31 ±0.02	-0.31 ±0.09
S(20)	60 K	0.72 ±0.04	-0.41 ±0.04	-0.47 ±0.02
	200 K	0.42 ±0.05	-0.36 ±0.04	-0.31 ±0.03

Table 6: Vector correlations for O_2 (a $^1\Delta_g$, v = 0) following the 282 nm photolysis of O_3 for a 60 K beam.

State	Temperature	$\beta_0^2(20)$	$\beta_0^0(22)$	$\beta_0^2(02)$
S(19)	60 K	0.55 ±0.07	-0.35 ±0.02	-0.50 ±0.05
S(20)	60 K	0.60 ±0.03	-0.38 ±0.02	-0.50 ±0.05

There is also no evidence for an alternation of the v-J correlation. For all the states except v = 1 at 248 nm, the v-J correlation is < -0.3. A value near limiting is expected for a triatomic dissociation. O_2 (a $^1\Delta_g$, v = 1, J = 31) has a v-J correlation of -0.28. This is the same state that showed a spatial anisotropy that is depolarized more than the even state. The signal was low so the results may not be reliable. The difference in v-J correlation between the even and odd states is shown in Figure 37. The results from the current study (circles) are compared to the work of Hancock *et al.*[3] (line). The error bars were generated by determining the largest error based on the error for the v-J correlation for the individual states. The line shows an increase in the difference between the v-J correlation as the speed of the fragments decreases. The current results do not show a significant difference. However, the majority of the fragments probed had large fragment speeds where Hancock *et al.* did not observe a large difference. The point at < 1000 m/s (v = 0 at 282 nm) shows a negligible difference in the v-J correlation (-0.071), however fragments with similar speeds from previous

studies show a significant difference. The previous studies were performed on ~140 K ozone. If the difference in the v-J correlation is dependent on parent internal energy, a v-J correlation difference may appear if the beam temperature is increased. It must be noted that for v = 0 at 282 nm, the odd state v-J correlation would have to be nearly 0 to obtain a difference that agreed with the previous work. For jet-cooled ozone, there does not appear to be a significant difference in the v-J correlation between even and odd states. If there is an alternation in the v-J correlation, it most likely is dependent on parent internal energy since no difference was observed for a cold beam and only appears for fragments with low speeds.

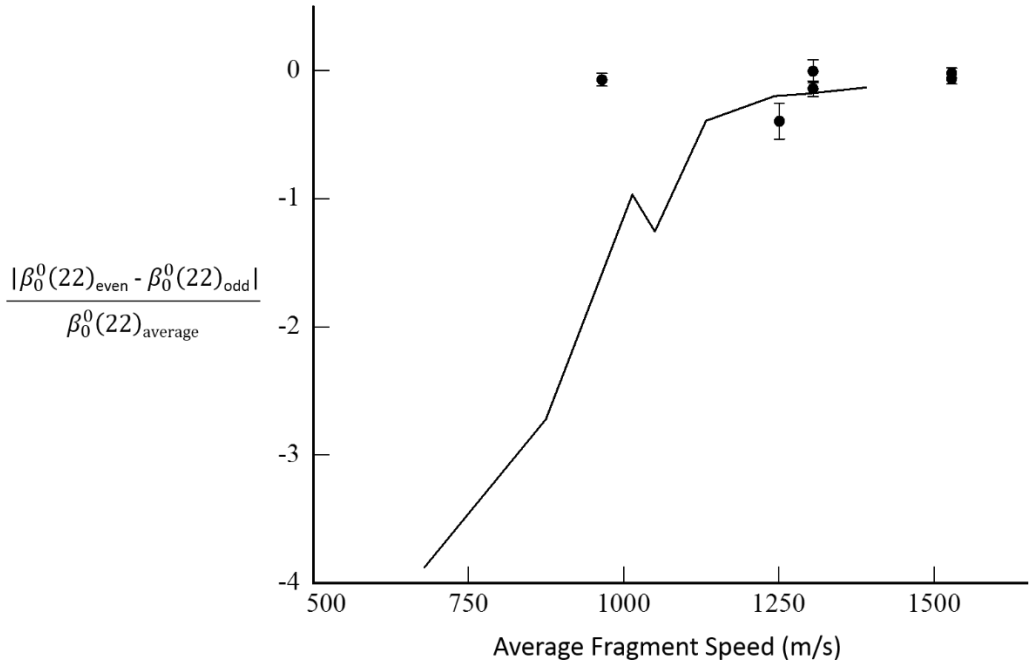

Figure 37: The difference in $\beta_0^0(22)$ (v-J correlation) between the even and odd J states with respect to the average fragment speed. The current results are shown with filled circles and the results from Ref. 3 is shown with a solid line.

Hancock *et al.*[3] state that the even and odd J states may arise from difference pathways. The even states belong to the O_2 (a $^1\Delta_g^+$) Λ doublet while the odd states belong to the O_2 (a $^1\Delta_g^-$) Λ doublet. If there are two pathways to form the different Λ doublets, then they may be affected by parent internal energy differently. For example, the $^1\Delta_g^-$ Λ doublet may be preferentially formed from parent molecules that have more out-of-plane motion. Since the out-of-plane motion depolarizes the v-J correlation, but does not affect the μ-v correlation, it would be expected that the μ-v correlation would be the same for both the even and odd states, but the v-J correlation would be more depolarized for the odd state. This is consistent with the observations from Hancock *et al.*[3] The degree of the depolarization effects could be dependent on the fragment speed as well. When the fragment speed is large, the impulse from the dissociation dominates and the depolarization effects from the parent are less significant. As the speed decreases, the parent rotational motion becomes more significant compared to the dissociation impulse and will have a larger effect. For a cold molecular beam, it has been shown in the previous chapter that the population for the odd states is lower compared to a warmer beam. The out-of-plane motion will be less excited for a colder beam, so perhaps there is no difference in the v-J correlation for cold ozone. As the internal energy is increased, the out-of-plane motion becomes more significant, more odd states are formed, and the difference in the v-J correlation is observed.

The current experiments have provided a new set of observations for the O_2 (a $^1\Delta_g$) vector correlations following the UV photolysis of ozone. The lack of alternation in

the v-J correlation between the even and odd states indicates that the difference may be dependent on parent internal energy. The observations are consistent with the odd rotational states preferentially being formed from warm parent molecules and may provide insight into the origin on the population alternation.

CHAPTER V

CONCLUSIONS AND FUTURE STUDIES

Despite numerous studies on the photodissociation of ozone in the Hartley band the dissociation dynamics continue to challenge experiment and theory. When ozone absorbs a UV photon, the dominant channel produces excited state fragments, O_2 ($a\ ^1\Delta_g$) + O (^{1}D). The O_2 ($a\ ^1\Delta_g$) vibrational distributions have been measured by multiple research groups and it has been found that the distribution is peaked at v = 0 and the population decreases monotonically with increasing vibrational state. The rotational distributions have not been studied in as great detail. Before the work in this dissertation, the rotational distributions have only been measured once using CARS. An interesting feature of the distributions is the even/odd J state intensity alternation. The odd state populations were lower relative to the even states. The strength of the alternation depended on O_2 v and J state as well as the photolysis wavelength.

The rotational envelopes obtained from the jet-cooled ozone experiments agree well with the CARS results. All the distributions are peaked at high J and the peak shifts to lower J with decreasing fragment speed. The main difference between the two sets of experimental results is the strength of the intensity alternation. For the ion imaging experiments, the alternation was much stronger compared to the CARS experiment. Also, the alternation did not have a large dependence on O_2 v state or photolysis wavelength. Due to the difference in temperatures between the two experiments, an

investigation of the effects of parent internal energy on the alternation was performed. It was found that by increasing the parent internal energy, the alternation in the (2, 0) band disappeared providing direct evidence that parent internal energy has a significant role in the population alternation.

Two explanations of the origin of the alternation have been proposed. Valentini *et al.*[13] explained the origin of the observed population alternation is due to a selective depletion of the odd states relative to the even states. Since only odd J states are allowed in the ground state of O_2, only odd states on the B state can couple to the R state and exit out the ground state channel. This leads to a suppression of odd states in the O_2 (a $^1\Delta_g$) rotational spectrum. Experiments were also performed with isotopically substituted ozone. The symmetry restrictions in the ground state for $^{16}O^{18}O$ are no longer valid and all rotational states are allowed. Therefore, all states can cross to the R state and the alternation should disappear. This is precisely what was observed. It was also shown that the even state populations were lower for $^{16}O^{18}O$ compared to $^{16}O^{16}O$ to prove the even states were allowed to cross.

Valentini and co-workers state that since the B/R curve crossing is the only pathway to form triplet products, the amount of suppression of the odd state is equal to the quantum yield of the triplet channel. If the B/R curve crossing was solely responsible for the alternation, the triplet quantum yield would be expected to track with the changes in the strength of the alternation. However, this is not the case. The alternation becomes weaker for longer photolysis wavelength while the triplet

quantum yield remains constant. The triplet quantum yield also does not depend on parent internal energy. The same triplet quantum yield was obtained for a jet-cooled and 300 K sample. A simple 1-D Landau-Zener model has been used to calculate the probability of crossing from the B to the R state. Based on this model, the velocity will dictate the crossing probability. Lower speeds would allow more fragments to cross to the R state and produce triplet products, increasing the triplet quantum yield and increasing the strength of the alternation in the singlet channel. This is opposite of what is observed in the CARS experiment. The alternation weakens as O_2 v state and photolysis wavelength increases, i.e. as the speed is decreased, there is less crossing to the R state and more odd J states are produced in the singlet channel.

An alternative explanation from Baloïtcha and Balint-Kurti[17] stated that the alternation is due to a preference for the even states and not a depeletion of the odd states. To explain the alternation, careful consideration of the form of both the initial wavefunction of the ozone precursor and the dissociatvie wavefunction of the molecule in its electronically excited state must be taken into account. For an ozone molecule with zero total angular momentum, these symmetry restrictions would only allow even J states in the excited O_2 rotational distribution. As the internal energy of ozone increases, the symmetry restrictions are relaxed and the odd J state population can increase. Presumably, at a certain point, the ozone molecule will have enough internal energy to relax the symmetry restrictions completely and no alternation due to the wavefunction symmetry restriction would be present.

The beam temperature studies indicate that parent internal energy is an important factor for the population alternation. Most likely, both explanations contribute to the intensity alternation. Since the curve crossing is the only pathway to form triplet products, it is correct that only odd states can cross to the R state which leads to a small depletion in the O_2 (a $^1\Delta_g$) rotational distribution. However, the trends observed in the alternation do not follow a curve crossing mechanism and it has been shown that parent internal energy affects the strength of the alternation. As the internal energy increases, symmetry restrictions are relaxed and the odd J state population is allowed to increase. The work of Picconi and Grebenshchikov[49] does not show any alternation, so there may be a third, unknown mechanism that is causing the population alternation.

The vector correlations provide more insight into the dissociation dynamics of ozone. No alternation in the v-J was observed between the even and odd J states. Although most of the states probed had relatively high fragment speeds. The v = 0 fragments following the 282 nm photolysis of ozone has much lower speeds, but still did not show a difference. That experiment was performed on 60 K ozone and perhaps a difference would appear for a warmer beam. If the odd states are dependent on the out-of-plane rotational motion of the parent molecules, the v-J values could be depolarized more than the even states that arise from rotation limited to the molecular plane. As the internal energy of the parent molecules is increased, there is more out-of-plane motion to form odd states and the motion will depolarize the v-J correlation

more than in plane motion. The effect is greater at lower fragment speeds because the dissociation impulse is lower so the torque from the parent becomes more significant.

5.1 Ozone Future Studies

The results described in this dissertation have helped elucidate the origin of the intensity alternation, but there are still questions that remain. The population alternation has been obtained for beam temperatures in the range of 60 – 200 K. It would be interesting to see how the alternation changes for temperatures outside of this range. To achieve a colder molecular beam, the orifice of the pulse valve could be smaller to produce a harder expansion. The alternation is already very strong in the (4, 0) band for a 60 K beam, but it would be interesting to see if the odd J state population decreases more producing a stronger alternation for a colder beam. Perhaps the odd states will not have any population. Alternatively, would the alternation weaken in the (4, 0) band for a molecular beam with a temperature of 300 K? The CARS experiment was performed at 300 K and the intensity alternation became weaker for higher O_2 vibrational state and at longer photolysis wavelengths. The dependence on O_2 v state and photolysis wavelength was not present for jet-cooled ozone. If the beam was warmed to 300 K, would the dependence on v state and photolysis wavelength be present?

Another experiment that would give more information about whether both of the explanations contribute to the population alternation would be to study isotopically

substituted ozone for a jet-cooled sample and detect the $^{16}O^{18}O$ fragment. Both even and odd rotational states are allowed in the ground state of O_2, so any alternation that is due to the curve crossing would disappear. Since the ozone molecules are jet-cooled, the symmetry restrictions due to the initial and dissociative wavefunctions might still cause a population alternation is the explanation is valid.

Extending the vector correlation study to slower fragment speeds may also provide information on the origin of the population alternation. Hancock *et al.*[3] observed a large difference in v-J values between even and odd states for slow fragments. This work obtained v-J values and did not observe a significant difference between the even and odd states. However, for fragments with similar speeds, Hancock and co-workers observed minor differences. Images at 282 nm for a cold beam did not show a significant difference in the v-J correlation between even and odd states. While fragments from Hancock and co-worker's study with similar speeds as the fragments from the photolysis of ozone at 282 nm showed a significant difference in v-J values. If v-J values were obtained for a warm beam following the 282 nm photolysis of ozone, would the difference between the v-J values become larger? If so, this would indicate that the even and odd states are affected by parent internal energy differently. If there are two pathways to form the even/odd J states, the odd states might preferentially arise from rotationally excited parent molecules.

Finally, in some of the measured images, an anisotropic ring was observed at larger radius than the O_2 (a $^1\Delta_g$) + O (^{1}D) signal shown in Figure 38 as the outer ring.

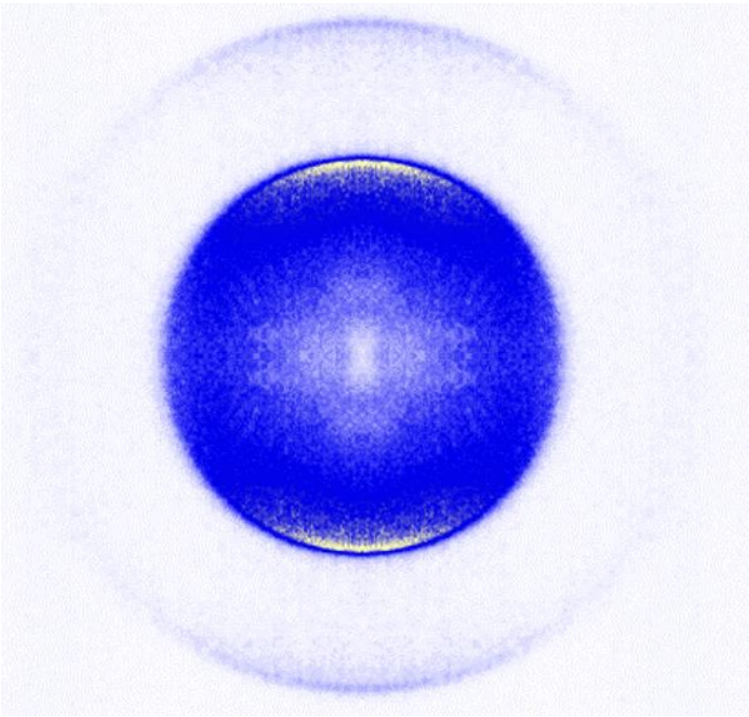

Figure 38: HV ion image of O_2 (a $^1\Delta_g$, v = 0, J = 19) from the S branch following the 266 nm photolysis of ozone. The outer ring is due to the spin-forbidden O_2 (a $^1\Delta_g$) + O (^{3}P) channel.

The intensity of the ring is much weaker. The large radius ring is most likely due to one-laser signal (~320 nm) of the spin-forbidden channel, O_2 (a $^1\Delta_g$) + O (^{3}P). The outer ring is anisotropic suggesting that the signal is only due to the vertically polarized probe laser for two reasons. Firstly, the signal is only dependent on the probe laser and secondly, the dissociation laser is horizontally polarized. If the signal was due to a two-laser process, no anisotropy is expected from the horizontally polarized laser. The radial distribution associated with the image in Figure 38 is shown in Figure 39. The radial distribution has had the background subtracted. The velocity of the spin-forbidden

channel is roughly the expected velocity for the O_2 fragment formed incoincident with the O (^{3}P) fragment for dissociation at ~320 nm. The calculated velocity is 2270 m/s while the experimental velocity is ~2100 m/s. The threshold for this channel is 195.78 kJ/mol.[63] The spin-forbidden channel from the photolysis of ozone in the Huggins band has been studied before[15, 63-66] and is expected to have a small quantum yield. The upper limit for the quantum yield of the spin-forbidden channel at ~320 nm is ~0.1.[63, 66] The formation of the spin-forbidden channel involves a crossing between the singlet R state with a triplet state that leads to O_2 (a $^1\Delta_g$) + O (^{3}P) products. Therefore, the model for the formation of spin-forbidden products first requires an internal conversion from the B to the R state and then an intersystem crossing to a triplet state.[65, 67] Studying the spin-forbidden channel may provide more information about the dissociation dynamics to help elucidate the origin of the population alternation in the O_2 (a $^1\Delta_g$) rotational distributions.

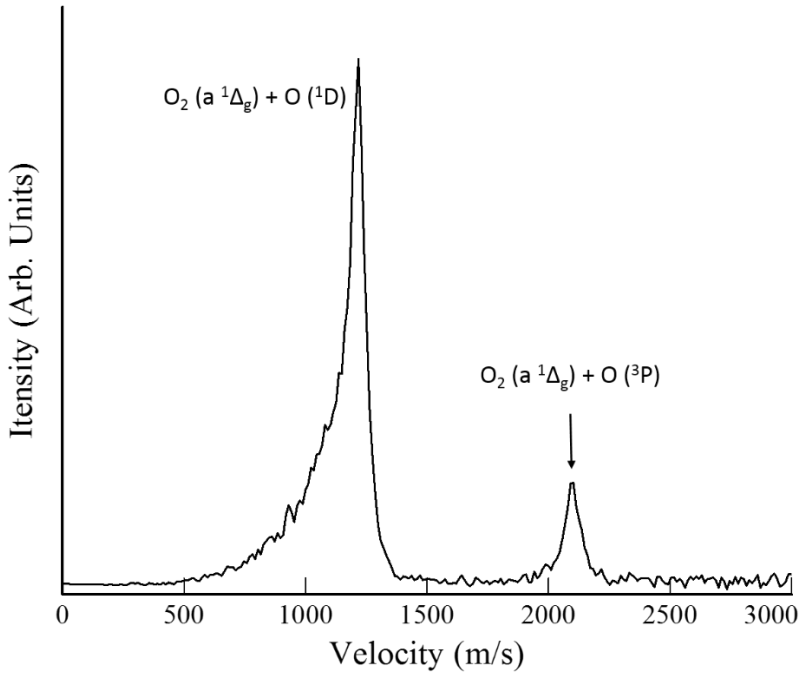

Figure 39: The radial distribution for v = 0, J = 19 of the O_2 (a $^1\Delta_g$) fragment. The arrow indicates the spin-forbidden channel.

5.2 CH_2NO_2 Future Studies

The roaming mechanism was first found to be important in the photodissociation of formaldehyde.[68, 69] The roaming mechanism is described as a frustrated atomic elimination pathway. One of the hydrogen atoms is stretched to long bond lengths, but is not able to break and form HCO + H. Instead, the hydrogen atom slowly roams around the remaining parent molecule for an extended time. Eventually, the hydrogen atom moves close to the parent molecule and abstracts the other H atom forming CO + H_2 products. The H_2 fragment is vibrationally excited since the bond was formed at a long bond length. The roaming mechanism is also present in the photolysis

of nitrate radical, NO_3.[70-73] In the NO_3 system, not only is roaming present, but two major discoveries were found that have never been observed before: roaming is the only pathway to form molecular products and roaming takes place on both the ground and excited states. For all other roaming systems, roaming only occurs on the ground state and there is a tight transition state that is the major pathway to form molecular products while roaming is a minor pathway. To date, the nitrate radical is still the only system to have these new features.

The nitromethyl radical, CH_2NO_2, is isoelectronic with NO_3 and has two dissociation channels: an atomic and molecular elimination channel. It has also been found that there are several low-lying electronic states.[74, 75] Since it is similar to NO_3, it is a system of interest to investigate whether it can only form molecular products via roaming and if roaming occurs on an excited state similar to NO_3. CH_2NO_2 UV photodissociation has been studied previously and the results showed some interesting features that were difficult to explain.[76] CH_2NO_2 dissociates to produce two product channels,

$$CH_2NO_2 \rightarrow CH_2NO + O \quad (5.1)$$

$$\rightarrow CH_2O + NO \quad (5.2)$$

The absorption cross section was found to be largest at 240 nm and decreased monotonically with increasing wavelength. The quantum yield for channel 5.2 increased with decreasing wavelength. Interestingly, no evidence was found for the simple C – N bond fission which is observed in the photodissociation of nitromethane,

CH_3NO_2. Channel 5.1 is produced with low translational energy (5 – 8 kcal/mol) which is expected from a simple bond rupture. However, the translational energy distribution for channel 5.2 is peaked at considerably higher energy (~60 kcal/mol) which indicates that either the barrier to dissociation is high or the potential energy is efficiently channeled into product kinetic energy. The minimum energy pathways to the two product channels is shown in Figure 40. The height of the barrier to form H_2CO + NO products is an estimate based on the fragment translational energy. The schematic is very similar to NO_3 so it is reasonable to predict that roaming plays an important role in the pathway to for molecular products. It was also suggested that dissociation to produce channel 5.2 occurs on an excited state. Determining the dissociation mechanism via a tight transition state to describe the results proved to be very difficult. Molecular elimination via roaming on an excited state could describe the experimental results.

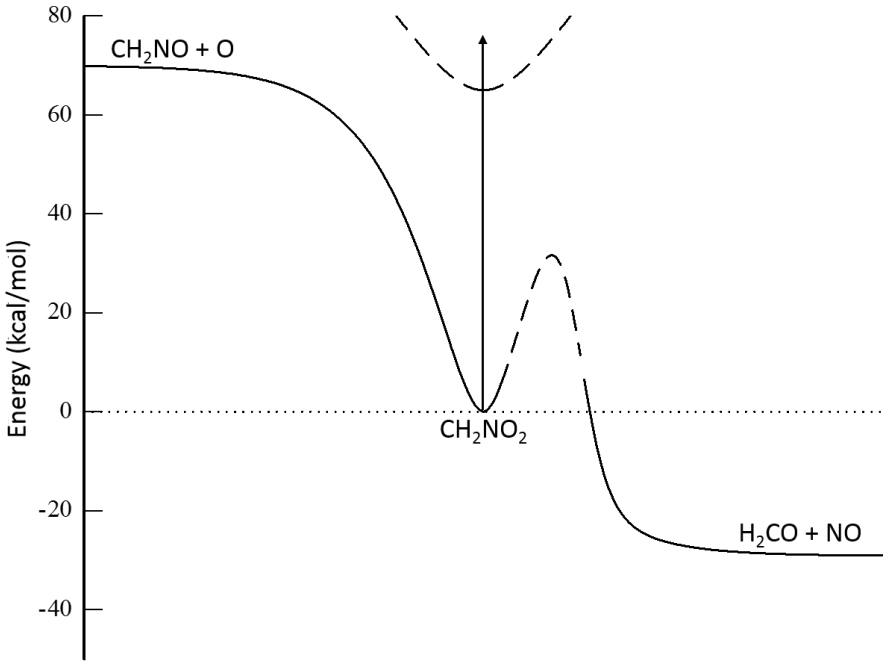

Figure 40: A schematic of the minimum energy pathways to the two product channels. The height of the barrier to H_2CO + NO products is unknown.

The nitromethyl radical is not stable and must be synthesized *in situ*, moments before it expands into the vacuum chamber. Kinetic simulations have already been performed and a synthesis method has been found. Ozone and nitromethane enter a mixing region in a dual pulse valve source. The mixing region is a quartz capillary tube. A 248 nm laser would enter the chamber through a quartz window at the back of the source chamber. The pulse valve source has a UV prism mounted on the side of the source where the laser would hit and be directed through the quartz mixing tube (Figure 41).

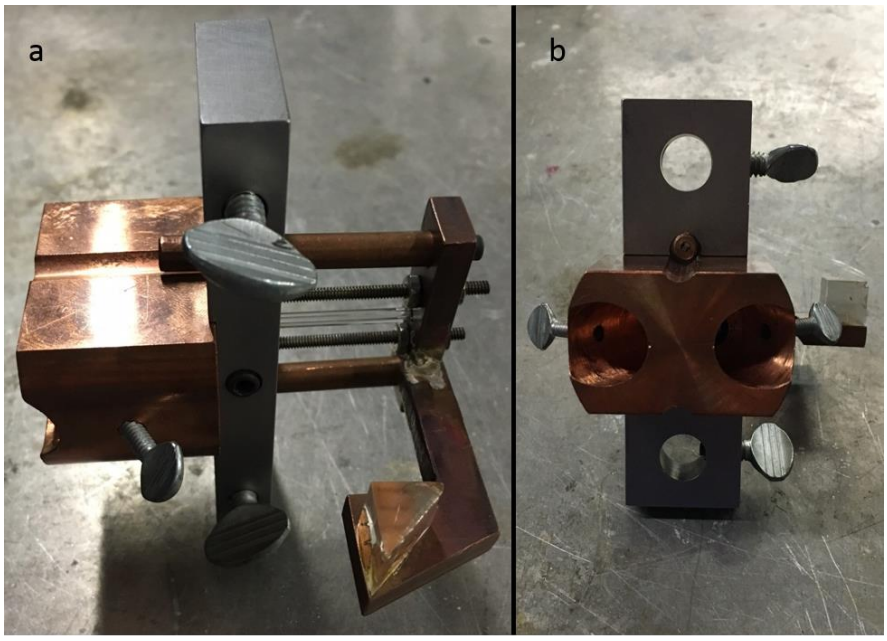

Figure 41: The dual-pulse valve source for the production of CH_2NO_2 radicals. a) A side view showing the location of the prism and quartz capillary tube b) back view showing the dual-pulse valve mounts.

Ozone will absorb a UV photon and dissociate to produce highly reactive, O (^{1}D) atoms. The O (^{1}D) atoms abstract a hydrogen atom from nitromethane, leaving the CH_2NO_2 radical. The resulting nitromethyl radical would then be launched via supersonic expansion into the chamber. Based on estimated pressures of 30 torr and 10 torr for CH_3NO_2 and O_3 respectively, the nitromethyl radical would reach an appreciable concentration in 0.2 μs (Figure 42). The photodissociation of CH_2NO_2 is not very well understood. The results from Cyr *et al.*[76] show striking similarities to NO_3. Before it was known that the roaming mechanism was the only pathway to molecular products, NO_3 photodissociation showed many of the same intriguing features as

CH_2NO_2 that were difficult to explain. The nitromethyl radical could very well be the second system to show roaming on an excited state where there is not an energetically available tight transition state for molecular elimination.

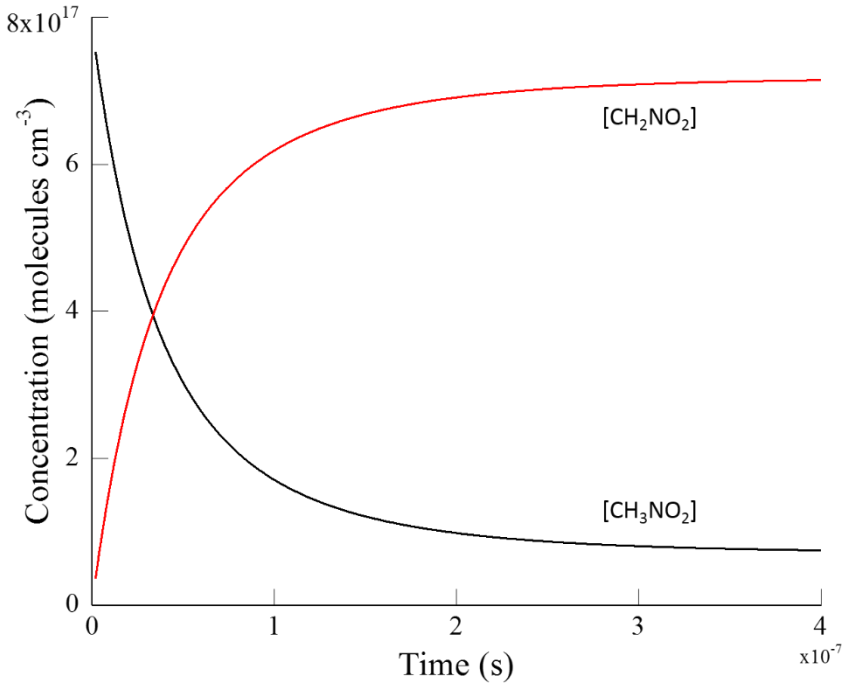

Figure 42: Kinetics simulation showing the concentrations of CH_3NO_2 and CH_2NO_2 over 0.4 µs

REFERENCES

[1] W. Denzer, S. J. Horrocks, P. J. Pearson, and G. A. D. Ritchie, Physical Chemistry Chemical Physics **8**, 1954-1962 (2006).

[2] S. M. Dylewski, J. D. Geiser, and P. L. Houston, The Journal of Chemical Physics **115**, 7460-7473 (2001).

[3] G. Hancock, G. A. D. Ritchie, and T. R. Sharples, Molecular Physics **111**, 2012-2019 (2013).

[4] S. J. Horrocks, G. A. Ritchie, and T. R. Sharples, The Journal of Chemical Physics **127**, 114308 (2007).

[5] S. J. Horrocks, G. A. D. Ritchie, and T. R. Sharples, The Journal of Chemical Physics **126**, 044308 (2007).

[6] Y. Matsumi, and M. Kawasaki, Chemical Reviews **103**, 4767-4781 (2003).

[7] R. L. Miller, A. G. Suits, P. L. Houston, R. Toumi, J. A. Mack *et al.*, Science **265**, 1831-1838 (1994).

[8] R. K. Sparks, L. R. Carlson, K. Shobatake, M. L. Kowalczyk, and Y. T. Lee, The Journal of Chemical Physics **72**, 1401-1402 (1980).

[9] D. Stranges, X. Yang, J. D. Chesko, and A. G. Suits, The Journal of Chemical Physics **102**, 6067 (1995).

[10] A. G. Suits, R. L. Miller, L. S. Bontuyan, and P. L. Houston, Journal of the Chemical Society, Faraday Transactions **89**, 1443-1447 (1993).

[11] K. Takahashi, N. Taniguchi, Y. Matsumi, and M. Kawasaki, Chemical Physics **231**, 171-182 (1998).

[12] M. A. Thelen, T. Gejo, J. A. Harrison, and J. R. Huber, The Journal of Chemical Physics **103**, 7946-7955 (1995).

[13] J. J. Valentini, D. P. Gerrity, D. L. Phillips, J. C. Nieh, and K. D. Tabor, The Journal of Chemical Physics **86**, 6745-6756 (1987).

[14] R. P. Wayne, Atmospheric Environment **21**, 1683-1694 (1987).

[15] S. M. Ball, G. Hancock, S. E. Martin, and J. C. Pinot de Moira, Chemical Physics Letters **264**, 531-538 (1997).

[16] C. E. Fairchild, E. J. Stone, and G. M. Lawrence, The Journal of Chemical Physics **69**, 3632-3638 (1978).

[17] E. Baloïtcha, and G. G. Balint-Kurti, The Journal of Chemical Physics **123**, 014306 (2005).

[18] E. Baloïtcha, and G. G. Balint-Kurti, The Journal of Chemical Physics **128**, 089901 (2008).

[19] F. Le Quéré, and C. Leforestier, The Journal of Chemical Physics **94**, 1118-1126 (1991).

[20] C. Leforestier, F. LeQuéré, K. Yamashita, and K. Morokuma, The Journal of Chemical Physics **101**, 3806-3818 (1994).

[21] S. Y. Lin, K. L. Han, and G. Z. He, The Journal of Chemical Physics **114**, 10651-10661 (2001).

[22] G. C. McBane, L. T. Nguyen, and R. Schinke, The Journal of Chemical Physics **133**, 144312 (2010).

[23] Z.-W. Qu, H. Zhu, S. Y. Grebenshchikov, and R. Schinke, The Journal of Chemical Physics **123**, 074305 (2005).

[24] Z.-W. Qu, H. Zhu, and R. Schinke, Chemical Physics Letters **377**, 359-366 (2003).

[25] R. Schinke, and G. C. McBane, The Journal of Chemical Physics **132**, 044305 (2010).

[26] M. Svanberg, J. B. C. Pettersson, and D. Murtagh, The Journal of Chemical Physics **102**, 8887-8896 (1995).

[27] M.-Y. Zhao, K.-L. Han, G.-Z. He, and J. Z. H. Zhang, Journal of Theoretical and Computational Chemistry **03**, 443-449 (2004).

[28] P. J. Hay, R. T. Pack, R. B. Walker, and E. J. Heller, The Journal of Physical Chemistry **86**, 862-865 (1982).

[29] EPA, (U.S. EPA, Office of Air and Radiation, Washington D.C., 2003).

[30] R. P. Wayne, *Chemistry of Atmospheres* (Oxford University Press, Oxford, UK, 2000).

[31] R. S. Stolarski, Scientific American **258**, 30 (1988).

[32] M. J. Newchurch, E.-S. Yang, D. M. Cunnold, G. C. Reinsel, J. M. Zawodny *et al.*, Journal of Geophysical Research: Atmospheres **108**, 4507 (2003).

[33] J. Austin, and N. Butchart, Quarterly Journal of the Royal Meteorological Society **129**, 3225-3249 (2003).

[34] I. Arnold, F. J. Comes, and G. K. Moortgat, Chemical Physics **24**, 211-217 (1977).

[35] J. C. Brock, and R. T. Watson, Chemical Physics **46**, 477-484 (1980).

[36] P. W. Fairchild, and E. K. C. Lee, Chemical Physics Letters **60**, 36-39 (1978).

[37] D. L. Philen, R. T. Watson, and D. D. Davis, The Journal of Chemical Physics **67**, 3316-3321 (1977).

[38] K. Takahashi, S. Hayashi, Y. Matsumi, N. Taniguchi, and S. Hayashida, Journal of Geophysical Research: Atmospheres **107**, ACH 11-11-ACH 11-18 (2002).

[39] M. Trolier, and J. R. Wiesenfeld, Journal of Geophysical Research: Atmospheres **93**, 7119-7124 (1988).

[40] R. H. Hughes, The Journal of Chemical Physics **24**, 131-138 (1956).

[41] J. S. Morrill, M. L. Ginter, E. S. Hwang, T. G. Slanger, R. A. Copeland *et al.*, Journal of Molecular Spectroscopy **219**, 200-216 (2003).

[42] J. S. Morrill, M. L. Ginter, B. R. Lewis, and S. T. Gibson, The Journal of Chemical Physics **111**, 173 (1999).

[43] W. J. van der Zande, W. Koot, J. Los, and J. R. Peterson, The Journal of Chemical Physics **89**, 6758 (1988).

[44] D. Manura, and D. Dahl, (Scientific Instrument Services, Inc., Ringoes, NJ, 2008).

[45] J. Lugue, and D. R. Crosley, (SRI International Report, 1999).

[46] S. Manzhos, and H.-P. Loock, Computer Physics Communications **154**, 76-87 (2003).

[47] D. Townsend, M. P. Minitti, and A. G. Suits, Review of Scientific Instruments **74**, 2530-2539 (2003).

[48] B. Whitaker, *Imaging in Molecular Dynamics* (Cambridge University Press, New York, 2003).

[49] D. Picconi, and S. Y. Grebenshchikov, The Journal of Chemical Physics **141**, 074311 (2014).

[50] R. G. Bray, and R. M. Hochstrasser, Molecular Physics **31**, 1199-1211 (1976).

[51] G. C. McBane, Private Correspondance, (2016).

[52] J. J. Valentini, Chemical Physics Letters **96**, 395-398 (1983).

[53] H. B. Levene, and J. J. Valentini, The Journal of Chemical Physics **87**, 2594-2610 (1987).

[54] J. J. Valentini, The Journal of Chemical Physics **86**, 6757-6765 (1987).

[55] J. C. Brock, and R. T. Watson, Chemical Physics Letters **71**, 371-375 (1980).

[56] R. N. Dixon, The Journal of Chemical Physics **85**, 1866-1879 (1986).

[57] R. N. Zare, and D. R. Herschbach, Proceedings of the IEEE **51**, 173-182 (1963).

[58] J. Solomon, The Journal of Chemical Physics **47**, 889-895 (1967).

[59] G. Hancock, S. J. Horrocks, P. J. Pearson, G. A. D. Ritchie, and D. F. Tibbetts, The Journal of Chemical Physics **122**, 244321 (2005).

[60] P. Andresen, G. S. Ondrey, B. Titze, and E. W. Rothe, The Journal of Chemical Physics **80**, 2548-2569 (1984).

[61] M. P. Grubb, M. L. Warter, C. D. Freeman, N. A. West, K. M. Usakoski *et al.*, The Journal of Chemical Physics **135**, 094201 (2011).

[62] M. D. Abramoff, P. J. Magalhaes, and S. J. Ram, Biophotonics International **11**, 36 (2004).

[63] W. Denzer, G. Hancock, J. C. Pinot de Moira, and P. L. Tyley, Chemical Physics **231**, 109-119 (1998).

[64] E. Silvente, R. C. Richter, M. Zheng, E. S. Saltzman, and A. J. Hynes, Chemical Physics Letters **264**, 309-315 (1997).

[65] H. Zhu, Z.-W. Qu, M. Tashiro, and R. Schinke, Chemical Physics Letters **384**, 45-51 (2004).

[66] S. M. Ball, G. Hancock, I. J. Murphy, and S. P. Rayner, Geophysical Research Letters **20**, 2063-2066 (1993).

[67] S. Y. Grebenshchikov, Z. W. Qu, H. Zhu, and R. Schinke, Physical Chemistry Chemical Physics **9**, 2044-2064 (2007).

[68] S. A. Lahankar, S. D. Chambreau, D. Townsend, F. Suits, J. Farnum *et al.*, The Journal of Chemical Physics **125**, 044303 (2006).

[69] D. Townsend, S. A. Lahankar, S. K. Lee, S. D. Chambreau, A. G. Suits *et al.*, Science **306**, 1158-1161 (2004).

[70] M. P. Grubb, M. L. Warter, K. M. Johnson, and S. W. North, The Journal of Physical Chemistry A **115**, 3218-3226 (2011).

[71] M. P. Grubb, M. L. Warter, and S. W. North, Physical Chemistry Chemical Physics **14**, 6733-6740 (2012).

[72] M. P. Grubb, M. L. Warter, A. G. Suits, and S. W. North, The Journal of Physical Chemistry Letters **1**, 2455-2458 (2010).

[73] M. P. Grubb, M. L. Warter, H. Xiao, S. Maeda, K. Morokuma *et al.*, Science **335**, 1075-1078 (2012).

[74] M. L. McKee, Journal of the American Chemical Society **107**, 1900-1904 (1985).

[75] R. B. Metz, D. R. Cyr, and D. M. Neumark, The Journal of Physical Chemistry **95**, 2900-2907 (1991).

[76] D. R. Cyr, D. J. Leahy, D. L. Osborn, R. E. Continetti, and D. M. Neumark, The Journal of Chemical Physics **99**, 8751-8764 (1993).

APPENDIX

VECTOR CORRELATION EQUATIONS

For a one photon dissociation and 2 + 1 REMPI, there are nine bipolar moments parameters, but three bipolar moments can be written as a linear combination of the other six bipolar moments. The linear combinations are shown in equations A.1 – A.3. The bipolar moments in A.4 – A.9 have been replaced with the corresponding linear combination. These equations were used in the forward convolution method to obtain vector correlations from the ion images. These equations are applicable to cases using 2 + 1 REMPI to probe the fragments.

$$\beta_0^2(42) = \frac{7}{12}\beta_0^2(02) - \frac{5}{12}\beta_0^2(22) \quad \text{(A.1)}$$

$$\beta_0^2(64) = \frac{11}{14}\beta_0^2(24) - \frac{3}{14}\beta_0^2(44) \quad \text{(A.2)}$$

$$\beta_0^0(44) = \frac{35}{18}\beta_0^0(22)^2 - \frac{5}{9}\beta_0^0(22) - \frac{7}{18} \quad \text{(A.3)}$$

$$\beta_2^{VV}=\frac{-[21075\beta_0^2(44)-107445\beta_0^2(24)-41650(\beta_0^0(22))^2+11900\beta_0^0(22)+8330]s_4-[85680\beta_0^2(22)-149940\beta_0^0(22)]s_2+149940\beta_0^2(20)}{59976\beta_0^2(02)s_2+74970}$$

(A.4)

$$\beta_4^{VV}$$

$$=\frac{-[100575\beta_0^2(44)-113625\beta_0^2(24)-603925(\beta_0^0(22))^2+172550\beta_0^0(22)+120785]s_4-[117810\beta_0^2(22)-164934\beta_0^2(02)]s_2}{109956\beta_0^2(02)s_2+137445}$$

(A.5)

$$\beta_6^{VV}=\frac{-[73725\beta_0^2(44)-247575\beta_0^2(24)-104125(\beta_0^0(22))^2+29750\beta_0^0(22)+20825]s_4}{94248\beta_0^2(02)s_2+117810}$$

(A.6)

$$\beta_2^{VH}$$

$$=\frac{-[4445\beta_0^2(44)-8407\beta_0^2(24)-4165(\beta_0^0(22))^2+1190\beta_0^0(22)+833]s_4-[2856\beta_0^2(02)-8568\beta_0^2(22)]s_2+11424\beta_0^2(20)}{[935\beta_0^2(44)+935\beta_0^2(24)+8330(\beta_0^0(22))^2-2380\beta_0^0(22)-1666]s_4+[-2856\beta_0^2(22)-2856\beta_0^2(02)-5712\beta_0^0(22)]s_2+5712}$$

(A.7)

$$\beta_2^{HV}=\frac{[55\beta_0^2(44)+55\beta_0^2(24)]s_4+[-252\beta_0^2(22)+84\beta_0^2(02)-336\beta_0^0(22)]s_2}{[11\beta_0^2(44)+11\beta_0^2(24)]s_4+[84\beta_0^2(22)+84\beta_0^2(02)]s_2+168\beta_0^2(20)-168}$$

(A.8)

$$\beta_4^{HV} = \frac{-[3462\beta_0^2(44) - 5106\beta_0^2(24) + 8330(\beta_0^0(22))^2 - 2380\beta_0^0(22) - 1666]s_4}{17[11\beta_0^2(44) + 11\beta_0^2(24)]s_4 + 17[84\beta_0^2(22) + 84\beta_0^2(02)]s_2 + 17[168\beta_0^2(20) - 168]}$$

(A.9)